Ubiquitous *CP* violation in a top-inspired left-right model

Ken Kiers,* Jeff Kolb,† and John Lee‡
Physics Department, Taylor University, 236 West Reade Avenue, Upland, Indiana 46989

Amarjit Soni§
High Energy Theory, Department of Physics, Brookhaven National Laboratory, Upton, New York 11973-5203

Guo-Hong Wu‖
Institute of Theoretical Science, University of Oregon, Eugene, Oregon 97403-5203
(Received 15 May 2002; published 8 November 2002)

We explore *CP* violation in a left-right-model that reproduces the quark mass and CKM rotation angle hierarchies in a relatively natural way by fixing the bidoublet Higgs VEVs to be in the ratio $m_b:m_t$. Our model is quite general and allows for *CP* to be broken by both the Higgs VEVs and the Yukawa couplings. Despite this generality, *CP* violation may be parametrized in terms of two basic phases. A very interesting feature of the model is that the mixing angles in the right-handed sector are found to be equal to their left-handed counterparts to a very good approximation. Furthermore, the right-handed analogue of the usual CKM phase δ_L is found to satisfy the relation $\delta_R \approx \delta_L$. The parameter space of the model is explored by using an adaptive Monte Carlo algorithm and the allowed regions in parameter space are determined by enforcing experimental constraints from the *K* and *B* systems. This method of solution allows us to evaluate the left-and right-handed CKM matrices numerically for various combinations of the two fundamental *CP*-odd phases in the model. We find that all experimental constraints may be satisfied with right-handed *W* and flavor changing neutral Higgs boson masses as low as about 2 TeV and 7 TeV, respectively.

DOI: 10.1103/PhysRevD.66.095002 PACS number(s): 12.60.−i, 11.30.Er, 12.15.−y

I. INTRODUCTION

The left-handedness of the observed weak interactions has long been a source of curiosity in particle physics. Left-right symmetry may be restored to the weak interactions at the Lagrangian level by introducing a new right-handed gauge boson. The aesthetic appeal of the so-called left-right model has led many to study it over the past few decades and the formal properties of the model are well known [1–11]. One feature that has emerged is that the new right-handed gauge boson must have a mass in the TeV range in order to evade the stringent bounds imposed by Δm_K [12]. This mass scale was unattainable two decades ago, but is now within reach, especially at upcoming colliders and perhaps also through precision studies of low-energy observables in the *B* system. Another factor that motivates a reexamination of the left-right model is that the model naturally accommodates nonvanishing neutrino masses as well as the enormous disparity in masses observed among the quarks and leptons. Indeed, very light neutrinos may be obtained through the seesaw mechanism, while the heaviness of the top quark may be reproduced through a judicious choice of vacuum expectation values (VEVs) in the extended Higgs sector of the model. The model is also able to account for the observed *CP* violation in the kaon and *B* systems and has additional possibilities for nonstandard *CP* violation through the presence of extra *CP*-odd phases. These phases appear, for example, in the right-handed analogue of the usual Cabibbo-Kobayashi-Maskawa (CKM) matrix [13,14] and are in addition to the single phase that appears in the usual CKM matrix.

While the formal properties of the left-right model are well known, its parameter space has not been studied exhaustively except in certain limiting cases. Two such cases are represented by the quasimanifest and pseudomanifest versions of the model. In the former, *CP* violation is present explicitly in the Yukawa couplings; in the latter, it arises spontaneously in the Higgs VEVs. In both of these cases the right-handed analogue of the usual CKM matrix is simplified in that the three right-handed rotation angles are identical to their left-handed counterparts. In the nonmanifest version of the model (considered in the present work), *CP* violation occurs in both the Higgs VEVs and the Yukawa couplings, and the right-handed CKM matrix can in principle be quite different from the left-handed one. In this case a full numerical solution needs to be undertaken in order to obtain detailed information regarding the right-handed sector of the model.

Detailed numerical results were first obtained for the left-right model in the early 1980s, mostly within the context of the pseudomanifest version of the model [15–18]. The authors of Ref. [19] improved upon earlier approximate methods of solution, while those of Refs. [20] and [21] imposed combined constraints coming from the neutral *K* and *B* systems. These latter works were all performed within the context of the pseudomanifest version of the model. To our knowledge, a detailed numerical solution of the nonmanifest case (*CP* violation in the Higgs VEVs and in the Yukawa

*Electronic address: knkiers@tayloru.edu
†Electronic address: jkolb@darkwing.uoregon.edu
‡Electronic address: john_lee@tayloru.edu
§Electronic address: soni@bnl.gov
‖Electronic address: gwu@darkwing.uoregon.edu

couplings), such as we present here, has not been performed. One important consideration in any numerical treatment of the left-right model concerns the flavor changing neutral Higgs (FCNH) boson that is generically present. The FCNH contribution to ϵ_K occurs at the tree level, leading in principle to a prohibitively large (of order 50 TeV [22]) lower bound on the Higgs boson mass scale. Our numerical study indicates that significantly lower values for the Higgs boson mass—on the order of 7 TeV—are actually tolerable.

In this paper we undertake a relatively exhaustive search of the parameter space of the left-right model, while making few assumptions regarding the structure of the model. Two main features distinguish the present work from that of previous authors. In the first place, we allow for *CP* violation both in the Yukawa couplings and in the Higgs VEVs (hence the ''ubiquitous'' in the title of this paper).[1] In the second, we employ a novel approach to the numerical solution of the problem, using a Monte Carlo algorithm to search the parameter space of the model. Our main assumption concerns the extended Higgs sector, where we take the bidoublet Higgs VEVs to be in the ratio $m_b:m_t$. This assumption is quite appropriate in the left-right model and leads very naturally to the observed hierarchy in the left-handed CKM matrix [15–17,19]. We also show that this assumption leads naturally to other attractive features of this model, namely that the rotation angles in the right-handed CKM matrix equal their left-handed counterparts to a good approximation and that the CKM phases δ_R and δ_L are approximately equal (see Appendix B). Note that while we shall always fix the ratio of the bidoublet Higgs VEVs, our method of solution is quite powerful and could easily be generalized to the case where the ratio is not $m_b:m_t$.

Throughout the present work we stress an important and general result that may not be widely known: assuming a minimal Higgs sector and three generations of quarks, the quark mass matrices in the left-right model depend on at most two nonremovable phases. This insight allows for the numerical solution of what might otherwise be a very complicated problem. Perhaps more importantly, the model contains only one new *CP*-odd degree of freedom beyond the one in the standard model (SM), a very desirable feature when comparing the model to forthcoming precision experimental results (particularly those coming from the *B* factories). In our notation, one of the *CP*-odd phases comes from one of the Higgs VEVs and the other is present in the Yukawa coupling matrices. The quasimanifest and pseudomanifest models may be recovered as limits of our model by setting one or the other of these two fundamental phases to zero or π.

The remainder of the paper is structured as follows. In Secs. II and III we outline our model and method of solution. Sections IV, V and VI discuss the various experimental constraints and show how these limit the parameter space of the model. Section VII contains some concluding remarks. In Appendix A we describe some details of our Monte Carlo algorithm. Appendix B contains a discussion of the relative sizes of the left-and right-handed CKM rotation angles as well as approximate expressions for the CKM phases δ_L and δ_R in terms of the fundamental parameters in the model.

II. THE MODEL

In this section we explain our notation and summarize some of the important formal aspects of our model. In particular, Sec. II B contains one of the central results of this paper, namely that many of the apparent degrees of freedom in the nonmanifest model may be eliminated by a suitably chosen unitary rotation. This insight leads to a considerable simplification of our task and allows us to proceed with our numerical work. For the purpose of the work to follow, we are mainly concerned with the Yukawa couplings between the quark and Higgs fields. The Higgs sector contains many intriguing features, including a flavor changing neutral Higgs boson and a doubly charged Higgs boson. Minimal versions of the model include a bidoublet Higgs field and a pair of either doublet or triplet Higgs fields. The triplet fields tend to be favored in the literature, since they can lead quite naturally to very light neutrino masses through the seesaw mechanism.

A. Quark mass matrices in the left-right symmetric model

Let us begin by deriving the relationship between the quark mass matrices and the left- and right-handed CKM matrices. In order to do so, we must first consider the Higgs fields. The left-right model is based on the gauge group $SU(2)_L \times SU(2)_R \times U(1)$, with the symmetry being spontaneously broken down to $U(1)_{\rm em}$ through the Higgs mechanism. The left- and right-handed quark fields transform as doublets under the unbroken gauge groups $SU(2)_L$ and $SU(2)_R$, respectively. The particular left-right model that we consider contains a bidoublet Higgs field $\Phi \sim (2,\bar{2},0)$ as well as two triplet Higgs fields $\Delta_L \sim (3,1,2)$ and $\Delta_R \sim (1,3,2)$,

$$\Phi = \begin{pmatrix} \phi_1^0 & \phi_2^+ \\ \phi_1^- & \phi_2^0 \end{pmatrix},$$

$$\Delta_{L,R} = \begin{pmatrix} \Delta_{L,R}^+/\sqrt{2} & \Delta_{L,R}^{++} \\ \Delta_{L,R}^0 & -\Delta_{L,R}^+/\sqrt{2} \end{pmatrix}. \tag{1}$$

The bidoublet field couples to the quarks and leptons and is responsible for giving them masses, while the right-handed triplet field is used to break the left-right symmetry at some high energy scale. The VEVs for these fields may be parametrized as follows:[2]

[1] When considering *CP* violation in the Higgs VEVs, we focus on the Higgs bidoublet and ignore the right-handed triplet, since the latter does not affect the quark mass matrices. See, for example, Ref. [11].

[2] Some authors use "$\delta_{L,R}$" for the VEVs of $\Delta_{L,R}$ but we prefer to reserve the symbols $\delta_{L,R}$ for phases appearing in the left- and right-handed CKM matrices.

$$\langle\Phi\rangle=\begin{pmatrix}\kappa & 0\\ 0 & \kappa'\end{pmatrix},\quad \langle\Delta_{L,R}\rangle=\begin{pmatrix}0 & 0\\ v_{L,R} & 0\end{pmatrix}. \tag{2}$$

In order to reproduce observed electroweak phenomenology, one typically assumes that $|v_R|\gg|\kappa|$, $|\kappa'|\gg|v_L|$, in which case κ and κ' satisfy the constraint [23]

$$|\kappa|^2+|\kappa'|^2\approx\frac{2m_W^2}{g^2}\approx(174.1\ \text{GeV})^2. \tag{3}$$

Although κ and κ' are both in principle complex, the only physically observable phase comes from their product, $\kappa\kappa'$. (One can always use a gauge rotation to eliminate the second phase.) We shall, for simplicity, take κ to be real and positive, so that the observable phase is carried by κ'; i.e.,

$$\alpha_{\kappa'}=\arg(\kappa'). \tag{4}$$

The Yukawa couplings of the quarks to the bidoublet Higgs fields may be written in terms of two 3×3 Hermitian matrices F and G as follows:

$$-\mathcal{L}_{\text{Yukawa}}=\overline{\psi'_{iL}}(F_{ij}\Phi+G_{ij}\tilde{\Phi})\psi'_{jR}+\text{H.c.}, \tag{5}$$

where $\tilde{\Phi}=\tau_2\Phi^*\tau_2$ and where the gauge eigenstates $\psi'_{iL,R}$ are given by

$$\psi'_{iL,R}=\begin{pmatrix}u'_{iL,R}\\ d'_{iL,R}\end{pmatrix}. \tag{6}$$

The Hermiticity of F and G helps ensure the left-right symmetry of the Lagrangian.[3] Insertion of the bidoublet Higgs VEVs into Eq. (5) yields the up- and down-type quark mass matrices

$$\mathcal{M}_u=\kappa F+\kappa'^*G \tag{7}$$

$$\mathcal{M}_d=\kappa' F+\kappa^* G. \tag{8}$$

$\mathcal{M}_u$ and $\mathcal{M}_d$ are, in principle, complex matrices, and may be diagonalized by biunitary transformations, yielding

$$\mathcal{M}_u^{\text{diag}}=V_L^{U\dagger}\mathcal{M}_u V_R^U \tag{9}$$

$$\mathcal{M}_d^{\text{diag}}=V_L^{D\dagger}\mathcal{M}_d V_R^D, \tag{10}$$

where $\mathcal{M}_u^{\text{diag}}\equiv\text{diag}(m_u,m_c,m_t)$ and $\mathcal{M}_d^{\text{diag}}\equiv\text{diag}(m_d,m_s,m_b)$. One can always choose the unitary rotation matrices $V_{L,R}^{U,D}$ in such a way that the elements of the diagonalized mass matrices are real and positive.

With the diagonalization matrices in hand, the charged-current Lagrangian may be written in terms of the (unprimed) quark mass eigenstates,

$$\mathcal{L}_{CC}=-\frac{g}{\sqrt{2}}\overline{u}_L V_L^{CKM}\gamma_\mu d_L W_L^{\mu+}-\frac{g}{\sqrt{2}}\overline{u}_R V_R^{CKM}\gamma_\mu d_R W_R^{\mu+}+\text{H.c.}, \tag{11}$$

where the generation indices have been suppressed and where we have taken the left- and right-handed weak coupling constants to be equal, $g_L=g_R\equiv g$. The left- and right-handed CKM matrices in the above expression are given by

$$V_L^{CKM}=B^\dagger V_L^{U\dagger}V_L^D\tilde{B} \tag{12}$$

$$V_R^{CKM}=B^\dagger V_R^{U\dagger}V_R^D\tilde{B}. \tag{13}$$

The matrices B and $\tilde{B}$ are diagonal phase matrices that are used to rotate as many phases as possible out of the left-handed CKM matrix (and hence into the right-handed CKM matrix), leaving V_L^{CKM} in its ''standard'' form with only one *CP*-violating phase δ_L [24],

$$V_L^{CKM}(\theta_{12},\theta_{23},\theta_{13},\delta_L)=\begin{pmatrix}c_{12}c_{13} & s_{12}c_{13} & s_{13}e^{-i\delta_L}\\ -s_{12}c_{23}-c_{12}s_{23}s_{13}e^{i\delta_L} & c_{12}c_{23}-s_{12}s_{23}s_{13}e^{i\delta_L} & s_{23}c_{13}\\ s_{12}s_{23}-c_{12}c_{23}s_{13}e^{i\delta_L} & -c_{12}s_{23}-s_{12}c_{23}s_{13}e^{i\delta_L} & c_{23}c_{13}\end{pmatrix}. \tag{14}$$

In the above expression, $s_{ij}\equiv\sin\theta_{ij}$, and all sines and cosines are taken to be non-negative. The left-handed phase δ_L is the usual CKM phase and is the sole source of *CP* violation within the context of the SM. It is also very nearly equal to the (perhaps more familiar) angle γ,

$$\delta_L\approx\gamma=\arg\left(-\frac{V_{L_{ud}}^{CKM}V_{L_{ub}}^{CKM*}}{V_{L_{cd}}^{CKM}V_{L_{cb}}^{CKM*}}\right). \tag{15}$$

With the above parametrization for V_L^{CKM}, V_R^{CKM} has six nonremovable phases. A convenient parametrization for V_R^{CKM} is as follows:

$$V_R^{CKM}=KV_L^{CKM}(\theta_{12}^R,\theta_{23}^R,\theta_{13}^R,\delta_R)\tilde{K}^\dagger, \tag{16}$$

where the right-handed rotation angles θ_{ij}^R are again taken to be in the first quadrant, so that all sines and cosines are non-negative. The diagonal matrices K and $\tilde{K}$ contain five of the six nonremovable phases in V_R^{CKM},

$$K=\text{diag}(e^{i\rho_1},e^{i\rho_2},e^{i\rho_3}) \tag{17}$$

$$\tilde{K}=\text{diag}(1,e^{i\eta_2},e^{i\eta_3}), \tag{18}$$

[3]See, for example, the discussion in Ref. [23].

with the sixth phase being δ_R, the right-handed analogue of δ_L. It is important to note that the seven nonremovable phases distributed among V_L^{CKM} and V_R^{CKM} are not, in general, all independent. In our model, for example, the seven phases are functions of only two ''basic'' phases [$\alpha_{\kappa'}$ and β_{23}; see Eqs. (4) and (21)].

There are several ways to achieve *CP* violation within the left-right model, and it is useful to enumerate these.

(1) *(Quasi)manifest left-right symmetry*. The simplest case occurs when *CP* is broken explicitly by the Yukawa couplings of the quarks to the Higgs fields. The product $\kappa\kappa'$ is real (so that $\alpha_{\kappa'}=0$ or π), but F and G (and hence the mass matrices themselves) are complex and Hermitian. In this case one has $V_{Rij}^{CKM}=\pm V_{Lij}^{CKM}$, a situation referred to as ''quasi-manifest left-right symmetry'' in Ref. [7]. ''Manifest left-right symmetry'' refers to the special case in which the ''+'' sign occurs for each of the nine elements of the matrices.

(2). *Pseudomanifest left-right symmetry*. One can also allow the product $\kappa\kappa'$ to carry the *CP*-violating phase and require F and G to remain real (and symmetric). In this case *CP* is broken spontaneously and the resulting mass matrices are complex symmetric. The left- and right-handed CKM matrices in this case satisfy the relation $V_R^{CKM}=AV_L^{CKM}*\tilde{A}^\dagger$, where A and $\tilde{A}$ are diagonal phase matrices; i.e., elements of the two matrices are equal in magnitude, but could have different phases. This case is often referred to as ''pseudomanifest left-right symmetry.''

(3). *Nonmanifest left-right symmetry*. In the most general case (considered in the present work), one allows both the product $\kappa\kappa'$ and the matrices F and G to be complex, while maintaining the Hermiticity of F and G. In this case, the mass matrices are in principle arbitrary complex matrices and the left- and right-handed CKM matrices have no special relations to each other. In particular, unlike in the previous cases, the rotation angles in V_L^{CKM} and V_R^{CKM} need not be equal. Many authors have considered the general case, and have made various *ansätze* for the form of V_R^{CKM}. Langacker and Sankar, for example, argued that a relatively light right-handed W could be accommodated if V_R^{CKM} took on one of the forms [23]

$$V_{R(A)}^{CKM}=\begin{pmatrix}1&0&0\\0&c&\pm s\\0&s&\mp c\end{pmatrix},\quad V_{R(B)}^{CKM}=\begin{pmatrix}0&1&0\\c&0&\pm s\\s&0&\mp c\end{pmatrix}. \tag{19}$$

The mixing angles in these expressions are clearly quite different from those of the left-handed CKM matrix.

In the present work we use the experimentally determined quark masses and left-handed rotation angles to delineate the various possibilities for the right-handed CKM matrix. We find that the right-handed rotation angles are very similar in magnitude to their left-handed counterparts (see Fig. 4 and Appendix B), ruling out the forms given in Eqs. (19), at least within the context of the class of models considered in this paper.

B. A top-inspired left-right model

In the present work we consider a particular version of the left-right model that is inspired by the relatively large masses of the third generation quarks as well as by the small mixing that exists between the third generation and the first two in V_L^{CKM}. It was pointed out many years ago that small 1–3 and 2–3 mixings follow naturally if one takes the ratio κ'/κ to be of order m_b/m_t [15–17,19]. This scenario was considered recently in the ''spontaneously broken left-right model'' (SB-LR), where the authors chose to fix the ratio at m_b/m_t [20,21],

$$\left|\frac{\kappa'}{\kappa}\right|=\frac{m_b}{m_t}. \tag{20}$$

The SB-LR is an example of a pseudomanifest left-right symmetric model. It contains many attractive features, such as spontaneous *CP* violation (arising from a single *CP*-odd phase) and upper limits on the Higgs and right-handed W masses. However, according to Ref. [20], the SB-LR predicts $\sin 2\beta_{CKM}^{\rm eff}\lesssim 0.1$. This value is difficult to reconcile with recent precision measurements, which give $\sin 2\beta_{CKM}^{\rm eff}=0.79\pm 0.11$ [25–27].[4] The SB-LR, although quite attractive, is somewhat tightly constrained because it does not allow for explicit *CP* violation in the Yukawa couplings. In the present work we retain the constraint given in Eq. (20), but generalize the mode of *CP* violation by allowing the Yukawa coupling matrices F and G to be (in principle) arbitrary 3×3 Hermitian matrices. At first glance it might appear that our generalization would hopelessly complicate matters by adding many new *CP*-odd phases. As we demonstrate below, however, it is possible to simplify the forms of F and G (without any loss of generality) in such a way that our model contains only one new phase compared to either the SB-LR or the SM [see Eq. (21) below].

It is useful to consider the number of degrees of freedom contained within the quark mass matrices, as well as the experimental constraints that may be placed on these. The most general expressions for the mass matrices in the left-right model are given in Eqs. (7) and (8), where κ is real, κ' is complex and F and G are Hermitian. The magnitudes of κ and κ' are fixed within our model [see Eqs. (3) and (20)] and the phase of κ has been gauged away. This leaves just one degree of freedom among κ and κ', namely the phase of κ'. Since F and G are both Hermitian 3×3 matrices, it would appear at first glance that there are a total of 18 degrees of freedom contained in F and G, for a total of 19 degrees of freedom within the quark mass matrices. It should be noted that six of these degrees of freedom would be new phases when compared to the SB-LR. On the experimental side,

[4]In determining the weighted average and its uncertainty, we use only the BABAR and BELLE results. The earlier Collider Detector at Fermilab (CDF) and CERN e^+e^- Collider LEP results are in agreement with the value we use. Inclusion of the CDF and LEP results would have only a very slight effect on the weighted average and its uncertainty.

there are nine direct constraints on the quark mass matrices (the so-called ''level I'' constraints below). These come from the six quark masses and the three left-handed rotation angles. The mass matrices would thus appear to be severely underconstrained, a situation that would not be ideal for a numerical study of the model. Fortunately, however, eight of the apparent degrees of freedom within F and G—including five of the six phases—may be rotated away by performing a unitary rotation in flavor space. This leaves 11 degrees of freedom with nine direct constraints placed upon them, a much more agreeable situation from the standpoint of solving the model numerically.

A rotation of all up, down, left and right quark fields by the same unitary matrix is unobservable, so one may perform the rotations $\mathcal{U}F\mathcal{U}^\dagger$ and $\mathcal{U}G\mathcal{U}^\dagger$ with no observable consequences. In particular, we can use $\mathcal{U}$ to diagonalize F, which yields all real eigenvalues (since F is Hermitian). It is also possible to change the overall signs of both F and G (simultaneously) with no observable consequences, so that a given element of the diagonalized version of F may always be taken to be positive. Having diagonalized F, we may perform a diagonal phase rotation (which does not affect F) in order to eliminate two phases in G. As a result, we may quite generally take F and G to be of the form

$$F=\begin{pmatrix} f_{11} & 0 & 0 \\ 0 & f_{22} & 0 \\ 0 & 0 & f_{33} \end{pmatrix},$$

$$G=\begin{pmatrix} g_{11} & g_{12} & g_{13} \\ g_{12} & g_{22} & g_{23}e^{i\beta_{23}} \\ g_{13} & g_{23}e^{-i\beta_{23}} & g_{33} \end{pmatrix}, \tag{21}$$

where all f_{ii} and g_{ij} are real, $f_{33}\geqslant 0$ and $g_{ij}\geqslant 0$ for $i\neq j$, and where the sole nontrivial phase, β_{23}, has (arbitrarily) been placed in the 2–3 element of G.[5] One may also assume without loss of generality that $f_{33}\geqslant|f_{22}|\geqslant|f_{11}|$. It should be emphasized that the forms given for F and G in Eq. (21) are completely general: the mass matrices of any left-right model (containing only a single bidoublet Higgs field) may be written in terms of only two *CP*-odd phases, which may be parametrized as $\alpha_{\kappa'}=\arg(\kappa')$ and $\beta_{23}=\arg(G_{23})$.[6]

[5]Note that if any of the off-diagonal elements of G are zero then the phase β_{23} may also be rotated away, yielding once again the pseudomanifest case.

[6]The results of the preceding few paragraphs are easily generalized to the case of N quark generations. In that case, if one wishes to put as few phases as possible in the left-handed CKM matrix, that number would be $(N-1)(N-2)/2$, leaving $N(N+1)/2$ nonremovable phases for the right-handed CKM matrix. Regarding ''fundamental'' or ''basic'' phases in the model, there would be 1 nonremovable phase among the bidoublet Higgs VEVs and $(N-1)(N-2)/2$ nonremovable phases in the Yukawa matrices. These latter phases could all be placed in ''G,'' as has been done in the present work.

Before proceeding to the numerical solution of our model, let us first obtain order-of-magnitude estimates for the elements of the Yukawa coupling matrices F and G. Our task is greatly simplified by the constraints in Eqs. (3) and (20). These imply, in an interesting coincidence, that

$$\kappa\sim\sqrt{\frac{2m_W^2}{g^2}}\approx 174.1\ \text{GeV}\sim m_t, \tag{22}$$

$$|\kappa'|\sim\frac{m_b}{m_t}\sqrt{\frac{2m_W^2}{g^2}}\sim m_b. \tag{23}$$

Consider first the expression given for $\mathcal{M}_u$ in Eq. (7). Since $\kappa\gg|\kappa'|$, we have, to a first approximation, that $\mathcal{M}_u\sim\kappa F$. (The elements of G do contribute somewhat to $\mathcal{M}_u$, but such contributions are suppressed by the small size of κ'.) Thus, to a first approximation one might expect

$$F\sim\begin{pmatrix} \mathcal{O}\left(\frac{m_u}{m_t}\right) & 0 & 0 \\ 0 & \mathcal{O}\left(\frac{m_c}{m_t}\right) & 0 \\ 0 & 0 & \mathcal{O}(1) \end{pmatrix}. \tag{24}$$

We will see below that the above hierarchy is indeed observed by the numerical solutions. The down quark mass matrix, $\mathcal{M}_d=\kappa' F+\kappa^* G$, yields insight both into the elements of G and into the sizes of the left- and right-handed rotation angles. Consider first the 3-3 element of $\mathcal{M}_d$. From Eqs. (23) and (24), we see that $\kappa' F_{33}$ is naturally of order m_b. If $\kappa^* G_{33}$ is also to be of order m_b, then G_{33} must be of order m_b/m_t. The other two elements of F give relatively small contributions to their respective down-type quark masses (since $\kappa' F_{ii}$ is ''too small'' in those two cases), so $\kappa^* G$ has primary responsibility for the masses of the first and second generation down-type quarks. This confirms our initial assertion that $\kappa'^* G$ would give a relatively small contribution to $\mathcal{M}_u$. To the extent that $\mathcal{M}_u\sim\kappa F$ is a good approximation, we have that V_L^U and V_R^U are approximately diagonal matrices. Thus V_L^{CKM} and V_R^{CKM} are essentially determined by V_L^D and V_R^D [see Eqs. (12) and (13)]. In a somewhat poorer approximation, we could also almost take $\mathcal{M}_d\sim\kappa^* G$, except for the 3-3 element. Noting that in our notation κ is real, we then have that $\mathcal{M}_d$ is ''almost'' Hermitian, except for its 3-3 element. If $\mathcal{M}_u$ and $\mathcal{M}_d$ were exactly Hermitian, then the left- and right-handed CKM matrices would have obeyed the ''quasimanifest'' condition noted above, $V_{Rij}^{CKM}=\pm V_{Lij}^{CKM}$. In practice, we find that the left- and right-handed rotation angles do agree reasonably well (see Fig. 4, below), that $\delta_R\approx\delta_L$ and that the right-handed phases corresponding to the first and second generations (ρ_1, ρ_2, and η_2) are all close to zero or π. The right-handed phases corresponding to the third generation (ρ_3 and η_3), by way of contrast, can take on any values. (See Fig. 3 below.) Appendix B contains some further discussion along these lines, along with approximate analytical relations for various CKM mixing angles and phases.

TABLE I. Values used in the determination of level I and II constraints. The first twelve rows correspond to the level I constraints, while the addition of the last five rows yields the level II constraints. The last two constraints are not included in the calculation of $\chi^2_{(II)}$, but are imposed as ''cuts'' after $\chi^2_{(II)}$ has satisfied the required tolerance. Quark masses are in GeV and are evaluated at the energy scale m_Z [28]; Δm_{B_d} is in ps^{-1}. Constraints 7–9 are taken from Ref. [20]. The central values, uncertainties and limits listed in this table are discussed in detail in Secs. IV and V.

i	y_i	Central value ($y_i^{\rm expt}$)	Uncertainty (σ_i) or limits
1	m_u	2.33×10^{-3}	0.45×10^{-3}
2	m_d	4.69×10^{-3}	0.66×10^{-3}
3	m_c	0.685	0.061
4	m_s	0.0934	0.0130
5	m_t	181	13
6	m_b	3.00	0.11
7	$\sin\theta_{12}$	0.2200	0.0030
8	$\sin\theta_{23}$	0.0395	0.0017
9	$\sin\theta_{13}$	0.0032	0.0008
10	m_u/m_d	0.497	0.119
11	m_s/m_d	19.9	3.9
12	$(m_s-(m_u+m_d)/2)(m_d-m_u)$	38.1	14.1
13	ϵ_K	2.28×10^{-3}	$[0.46+3.5\times(1.0\ \text{TeV}/M_2)^2]\times10^{-3}$
14	$\sin2\beta^{\rm eff}_{CKM}$	0.79	0.11
15	Δm_{B_d}	0.472	0.190
–	$\Delta m_{B_s}/\Delta m_{B_d}$	–	$\Delta m_{B_s}/\Delta m_{B_d}\geqslant27.2$
–	Δm_K	–	$-1\leqslant2\ \mathrm{Re}(M_{12}^{LR})/\Delta m_K^{\rm expt}\leqslant1$ and $\mathrm{Re}(M_{12})>0$

III. NUMERICAL SOLUTION OF THE MODEL—AN OVERVIEW

We turn now to a brief explanation of the numerical solution of our model. As noted above, the quark mass matrices in our model are described by eleven real ''input'' parameters: namely,

$$f_{ii}, g_{ij}\alpha_{\kappa'}, \text{ and } \beta_{23} \quad (11 \text{ input parameters}). \tag{25}$$

The model as a whole contains two more parameters—M_2 (the mass of the mostly right-handed heavy W) and M_H (the Higgs boson mass scale[7])—bringing the total number of ''input'' parameters in the model to thirteen. The goal of the numerical work is to find combinations of the various input parameters that yield acceptable values for quantities that are known experimentally, such as the quark masses, left-handed rotation angles and ϵ_K.

Each possible set of input parameters may be used to form trial mass matrices, which may then be diagonalized to yield the physical quark masses and the left- and right-handed CKM matrices, as described above in Sec. II A. The resulting quark masses and left-handed rotation angles (and possibly other quantities, such as ϵ_K, etc.) may then be compared to their known experimental values. A ''solution'' refers to a set of input parameters that satisfies all relevant experimental constraints to within some prescribed tolerance. In principle one could search the entire input parameter space for such solutions, but this is not possible in practice since the parameter space contains many dimensions, each of which contains a continuum of values. Fortunately, we can narrow down the parameter space to several promising regions by using the reasoning outlined in Sec. II B. But even with the parameter space pared down in this manner, it would still be very difficult (and inefficient) to find solutions by simply slicing up the multidimensional space into many small hypercubes. To overcome this problem we have devised an adaptive Monte Carlo routine (described in detail in Appendix A) that is able to zoom in on solutions with relatively high efficiency.

When discussing constraints satisfied by ''solutions'' in our model, it is useful to distinguish between minimal and higher-level constraints. Table I lists the various constraints employed. The twelve ''level I'' constraints take into account the quark masses and left-handed rotation angles, while the ''level II'' constraints include additional experimental inputs from the neutral kaon and B systems. Sections IV and V discuss these experimental constraints in detail. When the level I (or II) constraints have been satisfied to within the required tolerance, we call the set of input parameters a level I (or II) solution. In order to judge how close a given set of input parameters is to being a solution, we define a χ^2 for each of the constraints, and then sum these up to obtain a χ^2 for the appropriate constraint level; i.e.,

$$\chi_i^2=\frac{(y_i-y_i^{\rm expt})^2}{\sigma_i^2} \tag{26}$$

[7]We adopt the convention of several previous authors and assume that the various nonstandard physical Higgs bosons all have the same masses.

TABLE II. Ranges used for the input parameters. The various parameters are defined in Eqs. (4) and (21). The Monte Carlo procedure that searches for solutions takes the initial range for the ith parameter to be $x_{i,0}^{\rm cent} \pm \Delta_i$. The reader is referred to Appendix A for more details on the adaptive Monte Carlo algorithm.

i	x_i	Initial central value ($x_{i,0}^{\rm cent}$)	Initial range (Δ_i)
1	f_{11}	0	10^{-4}
2	f_{22}	0	0.03
3	f_{33}	1.04	0.25
4	g_{11}	0	3×10^{-4}
5	g_{22}	0	3×10^{-3}
6	g_{33}	0	0.06
7	g_{12}	10^{-3}	10^{-3}
8	g_{13}	10^{-3}	10^{-3}
9	g_{23}	0.01	0.01
10	$\alpha_{\kappa'}$	π	π
11	β_{23}	π	π

$$\chi^2_{(I)} = \sum_{i=1}^{12} \chi_i^2 \tag{27}$$

$$\chi^2_{(II)} = \chi^2_{(I)} + \sum_{i=13}^{15} \chi_i^2. \tag{28}$$

In these expressions $y_i^{\rm expt}$ represents the known ''experimental'' value for the ith constraint, y_i represents the value produced theoretically using the given set of input parameters and σ_i represents the uncertainty (experimental and/or theoretical) for the constraint. A set of input parameters is termed a solution if each of the relevant χ_i^2 is less than or equal to one. In the case of a level II solution, a few additional ''cuts'' must also be passed, as will be described below. Appendix A details the method by which our adaptive Monte Carlo routine attempts to minimize $\chi^2_{(I)}$ or $\chi^2_{(II)}$ as it searches the input parameter space for solutions.

Table II summarizes the ranges of the input parameters that yield viable values for the quark masses and left-handed CKM rotation angles. Denoting the various input parameters by x_i ($i=1,2,...,11$), we have found that solutions for each of the x_i lie within the range

$$x_{i,0}^{\rm cent} \pm \Delta_i, \tag{29}$$

where $x_{i,0}^{\rm cent}$ and Δ_i are given in the table. The ranges listed in the table correspond to the initial regions that the adaptive Monte Carlo algorithm uses as it searches for solutions. These ranges are consistent with the arguments made above in Sec. II B. (Note that the level I or II solutions themselves form a subspace of the regions indicated in the table.)

In the following three sections we discuss the two levels of constraint in detail and show the numerical results in each case. We also provide comparisons, where appropriate, with work performed by previous authors.

IV. LEVEL I CONSTRAINTS: QUARK MASSES AND ROTATION ANGLES

It is useful to begin by applying only the level I constraints, that is, only those constraints that involve the quark masses and left-handed CKM rotation angles in Table I. This analysis will help in the comparison to work performed by previous authors and will help clarify the mathematical structure of the model. Note that any level I solution may in principle be combined with values for M_2 and M_H (the masses of the predominantly right-handed gauge boson and the Higgs boson, respectively) and checked to see if the combination satisfies the level II constraints. This is not a particularly efficient method of finding level II solutions if M_2 and M_H are fixed at certain values, but does work reasonably well if many different pairs of masses are used.

Let us first discuss the level I constraints themselves. The quark masses and uncertainties listed in the table are evaluated at the scale m_Z [28]. These values were also used to determine the quark mass ratios and their uncertainties. The resulting ranges for the mass ratios are reasonably consistent with those quoted in Ref. [24], except that our range for the third ratio is somewhat larger than that quoted in Ref. [24]. The central values and uncertainties of the sines of the three rotation angles are taken from Ref. [20].

Since the input parameter space is multi-dimensional, we have found it convenient to display the regions of interest in a series of two- and three-dimensional projections. Figure 1 shows several such plots for level I solutions. It is clear from the plots that solutions exist for all values of $\alpha_{\kappa'}$ and β_{23}. This observation is consistent with our earlier discussion regarding the number of input parameters and constraints. Since we have 11 degrees of freedom and nine essential constraints,[8] we expect to have two unconstrained degrees of freedom. The remainder of the input parameter space is broken up into several disjoint regions. These regions actually shrink to a series of points as $\chi^2_{(I)}$ is reduced to zero.

Our numerical solutions provide an interesting point of contact with earlier work performed on the SB-LR [19,20], where it was pointed out that for each value of $\alpha_{\kappa'}$ there are 64 physically distinct solutions. In the SB-LR one can associate relative signs with the quarks masses, giving 32 different combinations. Another factor of ''2'' in that context comes from two possibilities for δ_L (close to zero or close to π). If our approach is correct and exhaustive, it should be able to find all 64 of these solutions. A good discriminator of the 64 solutions is the physically observable phase σ_d [defined in Ref. [20] and also in Eq. (34) below], which arises in B-$\bar{B}$ oscillations. Fixing $\alpha_{\kappa'}$ and setting $\beta_{23}=0$ and π (recall that F and G are real in the SB-LR) we have indeed found 64 distinct values for σ_d, in agreement with Ref. [20]. More generally, for any pair of values of the input phases $\alpha_{\kappa'}$ and β_{23} there appear to be 32 distinct solutions.

Figure 2 shows frequency plots of the various quark masses and rotation angles calculated using the input param-

[8]Note that the three quark mass ratios are ''redundant'' constraints in this context, although they are important in our numerical work.

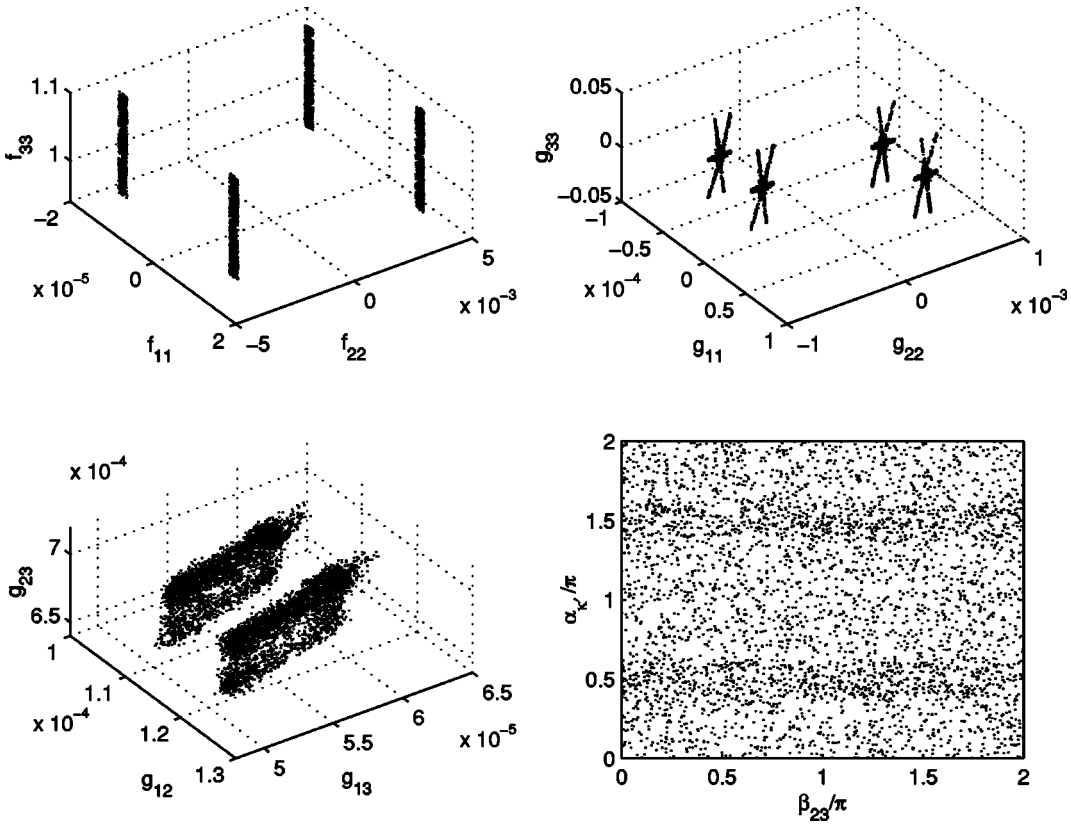

FIG. 1. Regions of the input parameter space yielding viable quark masses and left-handed mixing angles. For each $(\beta_{23},\alpha_{\kappa'})$ pair, the adaptive Monte Carlo procedure was used to find a set of values for the nine parameters f_{ii} and g_{ij} that satisfied the level I constraints. No extra constraints from the K or B systems have been imposed. The reader is referred to Appendix A for details concerning the numerical procedure used to find solutions.

eter sets displayed in Fig. 1. The dashed vertical lines in each plot represent the values $y_i^{\rm expt}\pm\sigma_i$. The histograms are entirely contained within the dashed lines since our numerical procedure ensures that all constraints are satisfied to within $\pm 1\sigma$. (We have opted for a somewhat restrictive approach in the present work, but one could easily relax the procedure.) Note that a narrower distribution indicates that the numerical procedure had a somewhat ''easier'' time satisfying the given constraint.

Figure 3 shows the various phases that characterize the left- and right-handed CKM matrices [see Eqs. (14)–(18)] for the input parameter sets plotted in Fig. 1. These plots may be regarded as ''predictions'' of our model in the sense that the points shown have passed all level I constraints. The plots show that all values are possible for δ_L (the sole phase in the left-handed CKM matrix) but that the right-handed phases are typically quite limited by the level I constraints. Inclusion of level II constraints will, of course, further limit the possible values that the left- and right-handed phases can assume (see Figs. 8 and 12 below, for example). One very interesting result in Fig. 3 is that δ_L is very closely tied to the fundamental phase β_{23} in G:

$$\delta_L \approx \beta_{23} + n\pi \pm 0.25 \ \text{ rad}, \tag{30}$$

where n is an integer and where the ''± 0.25 rad'' indicates the approximate spread of the values around $\beta_{23}+n\pi$. This result is consistent with the result found in Ref. [20], where F and G were taken to be real matrices ($\beta_{23}=0$ or π) and where two classes of solutions were found, one with $|\delta_L| \leqslant 0.25$ and the other with $|\delta_L-\pi|\leqslant 0.25$. Also interesting is the approximate equality between δ_L and δ_R evident in Fig. 3,

$$\delta_R \approx \delta_L \pm 0.50 \ \text{ rad}. \tag{31}$$

In order to understand this result, recall that in the quasimanifest case (real Higgs VEVs) one has the strict equality $\delta_R=\delta_L$, while in the SB-LR (real F and G) one has $\delta_R=-\delta_L$. In the latter case, one has the additional phenomenological result that $|\delta_L|\leqslant 0.25$ or $|\delta_L-\pi|\leqslant 0.25$, so that $|\delta_R-\delta_L|\leqslant 0.50$. Equation (31) may thus be viewed as a marriage of the results from these two cases: δ_R is approximately equal to δ_L, as in the quasimanifest case, but with a spread of ± 0.50, characteristic of the SB-LR. [Further discussion along these lines may be found in Appendix B, where Eqs. (30) and (31) are derived using an approximate analytical technique.] The remaining right-handed phases in Fig. 3 bear a very close resemblance to those one obtains in the SB-LR (obtained by restricting β_{23} to the values 0 and π). The quasimanifest limit itself is also evident in Fig. 3: the phases ρ_i and η_i reduce to 0 or π whenever $\alpha_{\kappa'}=n\pi$. This behav-

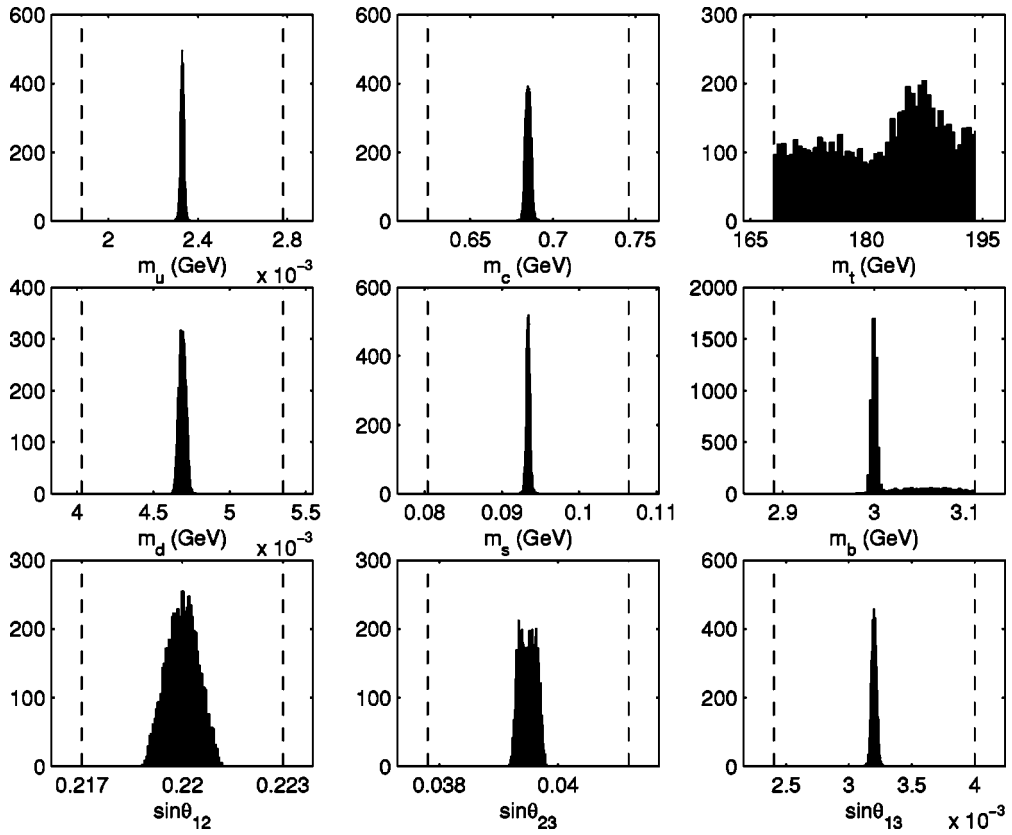

FIG. 2. Frequency spectrum of quark masses and rotation angles for the data set plotted in Fig. 1. The dashed vertical lines indicate the values $y_i^{\rm expt} \pm \sigma_i$. The vertical axis gives the number of observations in each bin.

ior is consistent with the known relation between the left- and right-handed CKM matrices in the quasimanifest case, namely $V_{Rij}^{CKM} = \pm V_{Lij}^{CKM}$ [7].

The ratio of right- to left-handed rotation angles (actually, their ''sines'') is shown in Fig. 4. The ratios are identically unity whenever $\alpha_{\kappa'}$ or β_{23} is equal to $n\pi$, since in these limits our model reduces to the quasimanifest or pseudomanifest case, respectively. In a general nonmanifest model the ratios are permitted to depart from unity, although our numerical results indicate that they do not do so by very much. The largest departure occurs for the ratio $\sin\theta_{13}^R/\sin\theta_{13}$, which is still typically within 20% of unity. The other two ratios are even closer to unity, with $\sin\theta_{23}^R/\sin\theta_{23}$ differing from unity by at most about 0.15%. In Appendix B we explain this intriguing agreement between the left- and right-handed rotation angles. In the case of the ratio of 2–3 angles, for example, the departure from unity is of order λ^5 (where $\lambda = 0.22$), which is in good agreement with our numerical results.

V. LEVEL II CONSTRAINTS: K-$\bar{K}$ AND B-$\bar{B}$ MIXING

The preceding section described the effects of imposing the level I constraints on our model. That analysis was useful in that it served to highlight some of the basic properties of the model. In the present section we describe the level II constraints, which are those coming from the neutral K and B systems. Section VI describes the effects of imposing these additional constraints, an endeavor that is complicated somewhat by the presence of two new degrees of freedom, namely the Higgs boson and W_2 masses. Table I contains a list of the level II constraints. These have been discussed in detail in Ref. [20] and also in Refs. [17] and [19]. Here we summarize some of the main results in those references. Note that we do not attempt to use ϵ' to place constraints on our results (except in Sec. VI A, below, where we compare our results with those found by previous authors within the SB-LR).

A. Experimental constraints from Δm_{B_d} and Δm_{B_s}

Δm_{B_d} and Δm_{B_s} can be quite sensitive to nonstandard contributions in the left-right model [18,20,29]. The off-diagonal terms in the mass matrices may be written in terms of a standard model piece and a left-right piece:

$$M_{12} = M_{12}^{SM} + M_{12}^{LR} = M_{12}^{SM}(1 + k_{d(s)} e^{i\sigma_{d(s)}}), \tag{32}$$

where

$$k_{d(s)} = \left|\frac{M_{12}^{LR}}{M_{12}^{SM}}\right| \approx \left|\frac{V_{R_{tb}}^{CKM} V_{R_{td(s)}}^{CKM*}}{V_{L_{tb}}^{CKM} V_{L_{td(s)}}^{CKM*}}\right| \left(\frac{B_B^{\rm scalar}}{B_B}\right) \times \left\{\left(\frac{7\ \ {\rm TeV}}{M_H}\right)^2 + \eta_2^{LR}\left(\frac{1.6\ \ {\rm TeV}}{M_2}\right)^2 \times \left[0.051 - 0.013 \ln\left(\frac{1.6\ \ {\rm TeV}}{M_2}\right)^2\right]\right\} \tag{33}$$

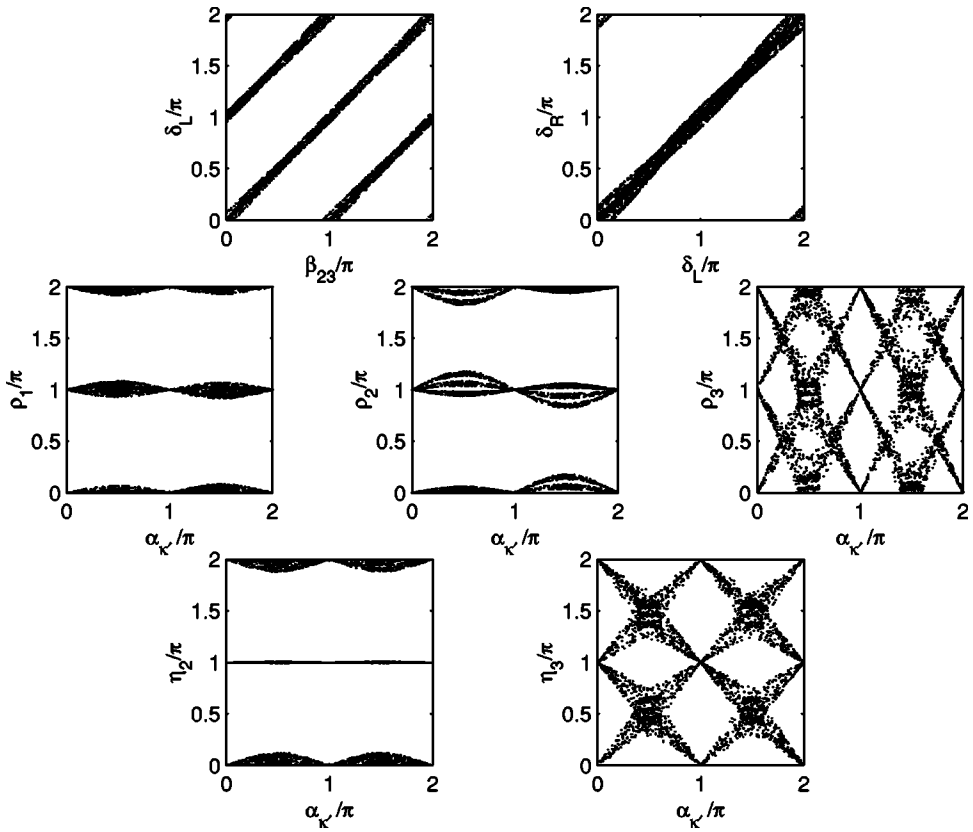

FIG. 3. Left- and right-handed CKM phases for the set of input parameters shown in Fig. 1. Note that the horizontal axes vary from plot to plot. Also, recall the definitions of the phases $\alpha_{\kappa'}$ and β_{23}: $\alpha_{\kappa'}=\arg(\kappa')$ and $\beta_{23}=\arg(G_{23})$.

and

$$\sigma_{d(s)}=\arg\left(-\frac{V_{R_{tb}}^{CKM}V_{R_{td(s)}}^{CKM*}}{V_{L_{tb}}^{CKM}V_{L_{td(s)}}^{CKM*}}\right), \tag{34}$$

with $B_B^{\text{scalar}}/B_B\simeq 1.2$ and $\eta_2^{LR}\simeq 1.7$ [20]. The expression for $k_{d(s)}$ is an approximation that is accurate to about 5% for $M_2>1.4$ TeV and $M_H>7$ TeV. The full expression for M_{12}^{SM} may be found in Ref. [20]. Our expression for $\sigma_{d(s)}$ is identical to that found in Ref. [20], while that for $k_{d(s)}$ differs in that it contains a ratio of right- and left-handed CKM matrix elements. This ratio is equal to unity in the spontaneously broken model considered in Ref. [20].

The above results may be used to solve for the B-$\overline{B}$ mass differences, since

$$\Delta m_{B_{d(s)}}=2|M_{12}|. \tag{35}$$

In the case of B_d, the mass difference is quite well known experimentally. Nevertheless, various theoretical uncertainties relax the bound somewhat, leading to the following constraint [20]:

$$|(V_{L_{tb}}^{CKM}V_{L_{td}}^{CKM*})^2(1+k_d e^{i\sigma_d})|=(6.7\pm 2.7)\times 10^{-5}. \tag{36}$$

In terms of Δm_{B_d} itself, the above range corresponds to $\Delta m_{B_d}=0.472\pm 0.190\ \text{ps}^{-1}$, as is quoted in Table II. In the case of B_s there is only an experimental lower bound on the mass difference, $\Delta m_{B_s}\geqslant 15.0\ \text{ps}^{-1}$ [30–33]. When comparing to theoretical expectations, the lower bound is usually

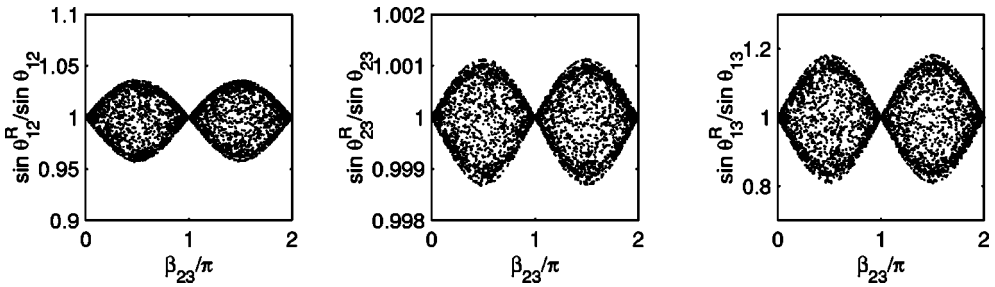

FIG. 4. Ratios of right- and left-handed rotation angles for the set of input parameters shown in Fig. 1.

TABLE III. Short-distance contributions to ϵ_K and Δm_K for a particular data point that satisfies all level I (but not level II) constraints. The left- and right-handed phases for this level I solution are $\delta_L = 0.9973$ and $(\rho_1, \rho_2, \rho_3, \eta_2, \eta_3, \delta_R) = (2.979, 0.1758, 3.168, 3.134, 4.783, 0.5801)$ and the sines of the right-handed rotation angles are $(\sin\theta_{12}^R, \sin\theta_{23}^R, \sin\theta_{13}^R) = (0.2254, 0.0396, 0.00279)$. We have set $\Lambda_3 = 0.350$ GeV, $\mu = 1.0$ GeV and $B_K = 0.86$.

M_2 (TeV)	M_H (TeV)	$\epsilon_K^{SD}/\epsilon_K^{\rm expt}$					$\Delta m_K^{SD}/\Delta m_K^{\rm expt}$				
		SM	FCNH	W_1W_2	S_1W_2	$W_1\Phi^\pm$	SM	FCNH	W_1W_2	S_1W_2	$W_1\Phi^\pm$
1.6	5	0.798	−31.9	−0.224	−1.61	−0.250	0.747	0.770	0.608	0.071	0.009
5	5	0.798	−31.9	−0.023	−0.249	−0.250	0.747	0.770	0.064	0.009	0.009
5	10	0.798	−7.98	−0.023	−0.249	−0.075	0.747	0.193	0.064	0.009	0.003
5	50	0.798	−0.319	−0.023	−0.249	−0.004	0.747	0.008	0.064	0.009	0.0001

expressed as a ratio, since this tends to decrease the theoretical uncertainty. We enforce the following bound:

$$\frac{\Delta m_{B_s}}{\Delta m_{B_d}} = 1.31 \times \left| \frac{(V_{L_{tb}}^{CKM} V_{L_{ts}}^{CKM*})^2 (1 + k_s e^{i\sigma_s})}{(V_{L_{tb}}^{CKM} V_{L_{td}}^{CKM*})^2 (1 + k_d e^{i\sigma_d})} \right| \geqslant 27.2. \tag{37}$$

This bound takes into account theoretical uncertainties and is slightly modified from that given in Ref. [20]. The Δm_{B_s} constraint is enforced in a different manner than most other constraints, since it is only included as a ''cut'' after a potential solution has been identified (i.e., Δm_{B_s} is not included in the evaluation of $\chi^2_{(II)}$).

B. Experimental constraints from ϵ_K and Δm_K

The K-$\overline{K}$ system has long played an important role in constraining the left-right model. Δm_K puts a lower bound of about 1.6 TeV on the mass of W_2 [12], while ϵ_K can in principle put a lower bound of about 50 TeV on the Higgs boson mass [22]. This latter bound is due to the presence of a tree-level FCNH contribution to ϵ_K. As we shall see in Sec. VI, a detailed numerical treatment of our model indicates that the experimental bounds may be satisfied with Higgs boson masses as low as about 7 TeV. Both ϵ_K and Δm_K are defined in terms of M_{12}, the off-diagonal term in the K-$\overline{K}$ mass matrix [20],

$$\epsilon_K = \frac{e^{i\pi/4}}{\sqrt{2}} \left(\frac{\mathrm{Im}(M_{12})}{\Delta m_K^{\rm expt}} + \xi_0 \right) \tag{38}$$

$$\Delta m_K = 2\,\mathrm{Re}(M_{12}), \tag{39}$$

where

$$\xi_0 = \frac{\mathrm{Im}\, a_0}{\mathrm{Re}\, a_0},$$

$$a_0^* = \langle \pi\pi(I=0) | -i\mathcal{H}_{\rm eff}^{|\Delta S|=1} | \overline{K^0} \rangle_{\rm weak}. \tag{40}$$

Δm_K suffers from relatively large theoretical uncertainties due to long-distance contributions, so we follow the usual practice of using the experimental value for Δm_K in Eq. (38) rather than the theoretical (short distance) expression obtainable from M_{12}. The term proportional to ξ_0 in Eq. (38) is also subject to considerable theoretical uncertainties. Within the SM these uncertainties do not pose any particular difficulties because the contribution due to this term is quite small and may safely be neglected. Such is not necessarily the case within the left-right model, where the contribution due to ξ_0 can be of order 30% for $M_2 = 1.6$ TeV [17,19,20]. We follow Ref. [20] in ignoring the ξ_0 contribution to ϵ_K and in taking its effect into account through a theoretical uncertainty.

Reference [17] contains a thorough discussion of the various contributions to M_{12} within the left-right model. Interestingly, the sum of box diagrams is not itself gauge invariant in the left-right model [34,35]. Nevertheless, the diagrams restoring gauge invariance give very small contributions in the 't Hooft–Feynman gauge, and can safely be ignored while working in that gauge. Similarly, several of the box diagrams generically give quite small contributions and can be ignored, leaving a total of five terms in the theoretical expression for M_{12} [17],

$$M_{12} = M_{12}^{SM} + M_{12}^{FCNH} + M_{12}^{W_1W_2} + M_{12}^{S_1W_2} + M_{12}^{W_1\Phi^\pm}, \tag{41}$$

where the first term is the usual SM contribution, the second corresponds to the tree-level FCNH contribution, and S_1 and $\Phi^\pm$ refer to one of the unphysical scalars and to the physical charged Higgs, respectively. (Recall that, for simplicity, all nonstandard Higgs bosons are taken to have the same mass in the present work.) Explicit expressions for the various terms may be found in Refs. [17] and [36] and are not included here.[9]

Table III shows a numerical evaluation of the five short-distance contributions to ϵ_K and Δm_K for a particular level I solution and gives a rough indication of how the various terms scale with increasing Higgs boson and W_2 masses. (There is nothing particularly ''special'' about this data point other than that it happens to give a SM contribution that is close to the known experimental value.) One of the most striking features of the table is the very large tree-level

[9]We use the NLO results in Ref. [36] for the SM piece and the LO results in Ref. [17] for the left-right pieces.

FCNH contribution to ϵ_K. Pospelov studied this contribution a few years ago in the case of manifest left-right symmetry and concluded that the corresponding Higgs boson would be required to have a mass in excess of 50 TeV [22]. The appropriateness of this bound is evident in the last row of the table, where the troublesome term is seen to reach a manageable size once $M_H \gtrsim 50$ TeV. Having said this, let us note that we are in fact able to find complete level II solutions with Higgs boson masses of order 7 TeV. Such solutions do require a certain amount of ''fine-tuning,'' but they exist nonetheless.

The left-right contributions to ϵ_K in Ref. [17] are only accurate to LO and display a relatively strong dependence on the low-energy QCD scales μ and Λ_3. The SM piece, while evaluated to NLO in the present work, is also subject to uncertainty due to the kaon bag parameter, B_K. In order to investigate the effects of these uncertainties, we have examined ϵ_K predictions for a set of data points that passed the level I constraints. We combined the data points with various Higgs boson and W_2 mass combinations and evaluated ϵ_K taking μ, Λ_3 and B_K in the ranges $\mu = 1.0 \pm 0.2$ GeV, $\Lambda_3 = 0.350 \pm 0.100$ GeV and $B_K = 0.86 \pm 0.15$. The resulting spread of ϵ_K values typically fell within 20–30 % of the mean. Rather than allowing these three parameters to vary in our numerical work, we have fixed them to the ''central'' values ($\mu = 1.0$ GeV, $\Lambda_3 = 0.350$ GeV and $B_K = 0.86$) and have assigned a 20% theoretical uncertainty to ϵ_K. Using the value $\epsilon_K = 2.28 \times 10^{-3}$ [24] and ignoring the small experimental uncertainty, we obtain[10]

$$\epsilon_K = [2.28 \pm (0.46 + 3.5 \times (1.0 \ \text{TeV}/M_2)^2)] \times 10^{-3}, \tag{42}$$

where the first term in the uncertainty is due to uncertainties in μ, Λ_3 and B_K. The second term in the uncertainty is due to our neglect of the ξ_0 term in Eq. (38) and is taken from Ref. [20].

Theoretical expressions for Δm_K involve large uncertainties due to long distance contributions, even within the context of the SM. The SM calculation of the short-distance contribution to Δm_K gives roughly 70% of the known experimental value (see Table III). Within the SM, the remaining 30% is thought to be due to long-distance effects. It is not clear how one might best use Δm_K to place constraints on nonstandard physics, since the long-distance contributions are somewhat unknown. We follow previous authors and constrain new contributions to be at most as large as Δm_K^{expt} itself. Our constraints are

$$-1 \leqslant 2\,\text{Re}(M_{12}^{LR})/\Delta m_K^{\text{expt}} \leqslant 1 \quad \text{and} \quad \text{Re}(M_{12}) > 0. \tag{43}$$

[10]We have used $N_f = 3$ when evaluating the expressions in Ref. [17]. In some of the expressions (such as in the treel-level FCNH contribution) one could in principle evolve the Wilson coefficients in several steps rather than all at once, but it is not clear that this would be appropriate in some of the other expressions.

The Δm_K constraints are implemented as cuts and are not used in the evaluation of $\chi^2_{(II)}$.

C. Experimental constraint from $B \to \psi K_S$

Recent measurements of $\sin 2\beta_{CKM}^{\text{eff}}$ by the BABAR and BELLE Collaborations yield the values $0.59 \pm 0.14 \pm 0.05$ and $0.99 \pm 0.14 \pm 0.06$, respectively [25,26]. Taking the weighted average yields the value $\sin 2\beta_{CKM}^{\text{eff}} = 0.79 \pm 0.11$, which is consistent with the slightly older CDF measurement [27]. This experimental value actually acts to constrain both the CKM angle ''β_{CKM},'' as well as nonstandard effects coming from K-$\bar{K}$ and B-$\bar{B}$ mixing. The full theoretical expression is given by [20]

$$\sin 2\beta_{CKM}^{\text{eff}} = \sin\left[2\beta_{CKM} + \arg(1 + k_d e^{i\sigma_d}) - \arg\left(1 + \frac{M_{12}^{K,LR}}{M_{12}^{K,SM}} \right) \right], \tag{44}$$

where

$$\beta_{CKM} = \arg\left(-\frac{V_{L_{cd}}^{CKM} V_{L_{cb}}^{CKM*}}{V_{L_{td}}^{CKM} V_{L_{tb}}^{CKM*}} \right). \tag{45}$$

When employing $\sin 2\beta_{CKM}^{\text{eff}}$ as a constraint we take into account the experimental uncertainty, but do not include any additional theoretical uncertainty.

VI. LEVEL II SOLUTIONS: NUMERICAL RESULTS

In this section we employ all the experimental constraints in Table I in order to search the parameter space of the model for level II solutions. Section VI A contains a study of our model in the pseudomanifest limit (F and G real), in which case our model reduces to the SB-LR [20]. In Secs. VI B and VI C we perform two case studies. In the first we fix the W_2 and Higgs boson masses to be 5 and 10 TeV, respectively, while in the second we allow the masses to vary over prescribed ranges.

A. Comparison with results in the SB-LR

We begin by using our method to rederive some of the results obtained in the SB-LR [20], since this serves as a useful check of our method. Figure 5 shows plots of $\Delta m_{B_d}/\Delta m_{B_d}^{\text{expt}}$, $\Delta m_{B_s}/\Delta m_{B_s}^{SM}$ and $\sin 2\beta_{CKM}^{\text{eff}}$ for a set of level I solutions generated for a particular value of the phase $\alpha_{\kappa'}$, where [20]

$$\frac{\Delta m_{B_d}}{\Delta m_{B_d}^{\text{exp}}} = \frac{|(V_{L_{tb}}^{CKM} V_{L_{td}}^{CKM*})^2 (1 + k_d e^{i\sigma_d})|}{(6.7 \times 10^{-5})} \tag{46}$$

$$\frac{\Delta m_{B_s}}{\Delta m_{B_s}^{SM}} = \frac{|(V_{L_{tb}}^{CKM} V_{L_{ts}}^{CKM*})^2 (1 + k_s e^{i\sigma_s})|}{0.039^2}. \tag{47}$$

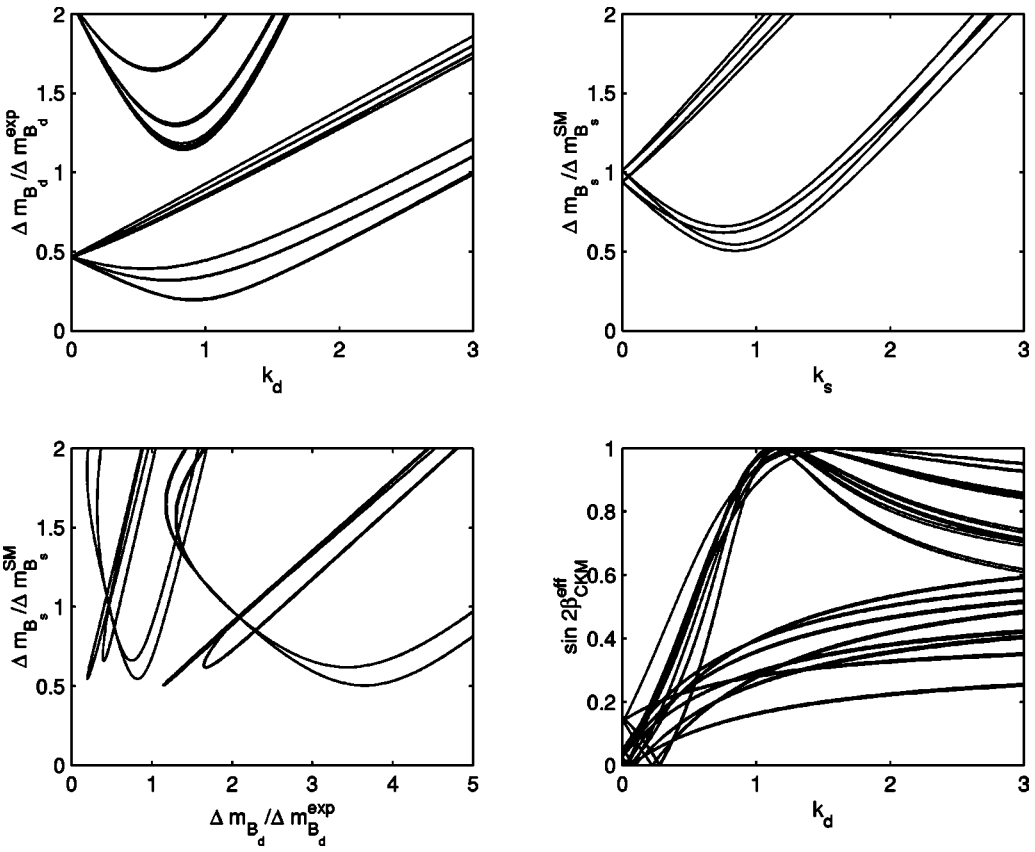

FIG. 5. Reproduction of some results obtained for the SB-LR in Ref. [20]. The above plots were obtained by setting $\beta_{23}=0,\pi$ and $\alpha_{\kappa'}=\sin^{-1}((1-r^2)\tan\beta/(2r))$, with $r=|\kappa'/\kappa|$ and $\beta=0.02$, in the notation of Ball *et al.* The plots may be compared with the $\beta=0.02$ case in each of Figs. 4–7 in Ref. [20]. Note that $k_s=k_d$ in the SB-LR, since the ratio of CKM matrix elements in Eq. (33) is equal to unity in that case. Note also that the above plot of $\sin 2\beta_{CKM}^{\rm eff}$ neglects the $K-\overline{K}$ mixing contribution, as does the analogous plot in Ref. [20]. Only non-negative values of $\sin 2\beta_{CKM}^{\rm eff}$ are shown.

In each case the plot was obtained by allowing β_{23} to take on the values 0 and π, since our model reduces to the SB-LR for these values of β_{23}. In order to reproduce the results of Ball *et al.* more precisely, we have enforced the rather stringent bound $\chi^2_{(I)}<2\times10^{-6}$ for this particular set of points. Comparison of this figure with Figs. 4–7 in Ref. [20] shows quite good agreement of our results with those obtained there. There are, however, two differences between our results and those in Ref. [20]. In the first place, the overall shapes of the plots are slightly different. This difference is due to a slightly different choice of quark masses and left-handed rotation angles. A second difference concerns the number of lines evident in the plots. In some places where we appear to have a single line (or several very closely spaced lines), Ball *et al.* have several lines. One possibility would be that our method is actually missing some solutions. We do not believe this to be the case, however, since our evaluation of σ_d for this case shows 64 distinct values. The reason for this difference is not clear to us.

We may also draw a comparison with Fig. 9 in Ref. [20], which shows a plot of ϵ_K versus $\sin 2\beta_{CKM}^{\rm eff}$ for a range of values for M_2 and M_H. Figure 6 shows two plots of ϵ_K versus $\sin 2\beta_{CKM}^{\rm eff}$ for the case when $\beta_{23}=0,\ \pi$. For each of the plots a set of level I solutions is combined with many pairs of W_2 and Higgs boson masses. The points shown have passed the Δm_{B_d}, Δm_{B_s} and Δm_K bounds in Table I[11] and correspond to masses in the range $2<M_2<16$ TeV and $4<M_H<18$ TeV. The plot on the right has passed an additional cut on $\epsilon'=\epsilon'_{SM}+\epsilon'_{LR}$. In evaluating ϵ', we have taken the SM piece from Ref. [36]. For the LR piece we have used the following expression [19]:

$$\epsilon'_{LR}\simeq e^{i\pi/4}\times10^{-2}\times\left\{\left[6.8\left[\frac{\alpha_s(\mu^2)}{\alpha_s(M_2^2)}\right]^{-2/b}-0.30\right.\right.$$
$$\left.\times\left[\frac{\alpha_s(\mu^2)}{\alpha_s(M_2^2)}\right]^{4/b}\right]\frac{M_1^2}{M_2^2}\sin(-\eta_2)+102\zeta$$
$$\times[\sin(\alpha_{\kappa'}+\rho_1-\eta_2)+\sin(\alpha_{\kappa'}+\rho_1)]-9.6\zeta$$
$$\left.\times[\sin(\alpha_{\kappa'}+\rho_2)+\sin(\alpha_{\kappa'}+\rho_2-\eta_2)]\right\},\qquad(48)$$

where

[11]When comparing with the SB-LR we began with level I solutions and enforced all level II constraints as "cuts."

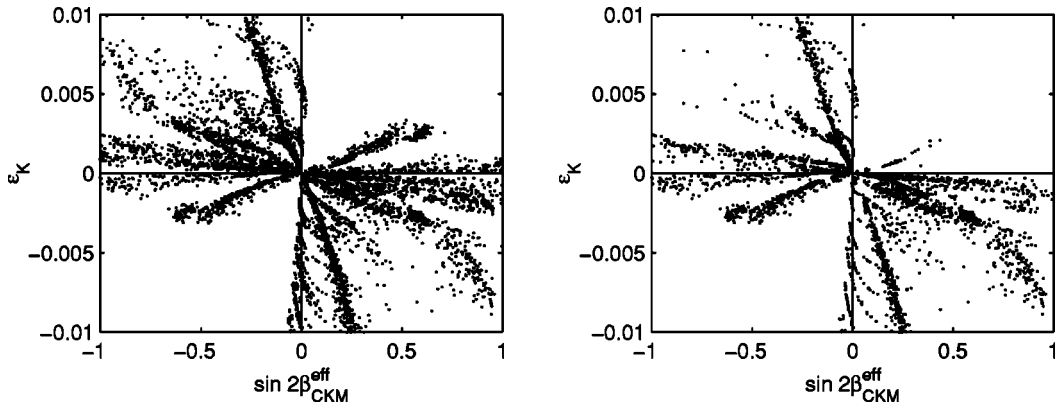

FIG. 6. Plot of ϵ_K versus $\sin 2\beta^{\rm eff}_{CKM}$ in the SB-LR. The plot on the left satisfies all Δm-type bounds (as described in the text). The plot on the right satisfies the additional constraint $e^{-i\pi/4}\epsilon' > 0$ and may be compared with Fig. 9 in Ref. [20].

$$\zeta = \frac{2r}{1+r^2}\left(\frac{M_1}{M_2}\right)^2, \tag{49}$$

with $r = |\kappa'/\kappa|$ and $b = 11 - 2N_f/3$. The above expression for ϵ'_{LR} has been modified from that in Ref. [19] in order to account for a slight difference in gauge choice with respect to the phases of the bidoublet Higgs VEVs.

Comparison of Fig. 6 in the present work with Fig. 9 in Ref. [20] shows reasonable agreement between the two plots, but there are a few differences. In particular, while Ball *et al.* find no solutions near the experimental values for ϵ_K and $\sin 2\beta^{\rm eff}_{CKM}$, we do find solutions that are somewhat close to these values. Also, while Ball *et al.* have very few points in the third quadrant, our plot shows a fairly prominent band in this region. It is unclear to us why our results differ from those found by Ball *et al.*, particularly given the good agreement between our Fig. 5 and their Figs. 4–7. It is possible that the discrepancy is due to small differences in our evaluation of the expressions for ϵ_K or Δm_K in Ref. [17] or in our evaluation and application of the ϵ' constraint. We should emphasize that, due to the significant theoretical uncertainties involved in the calculation of ϵ', we do not use ϵ' in the

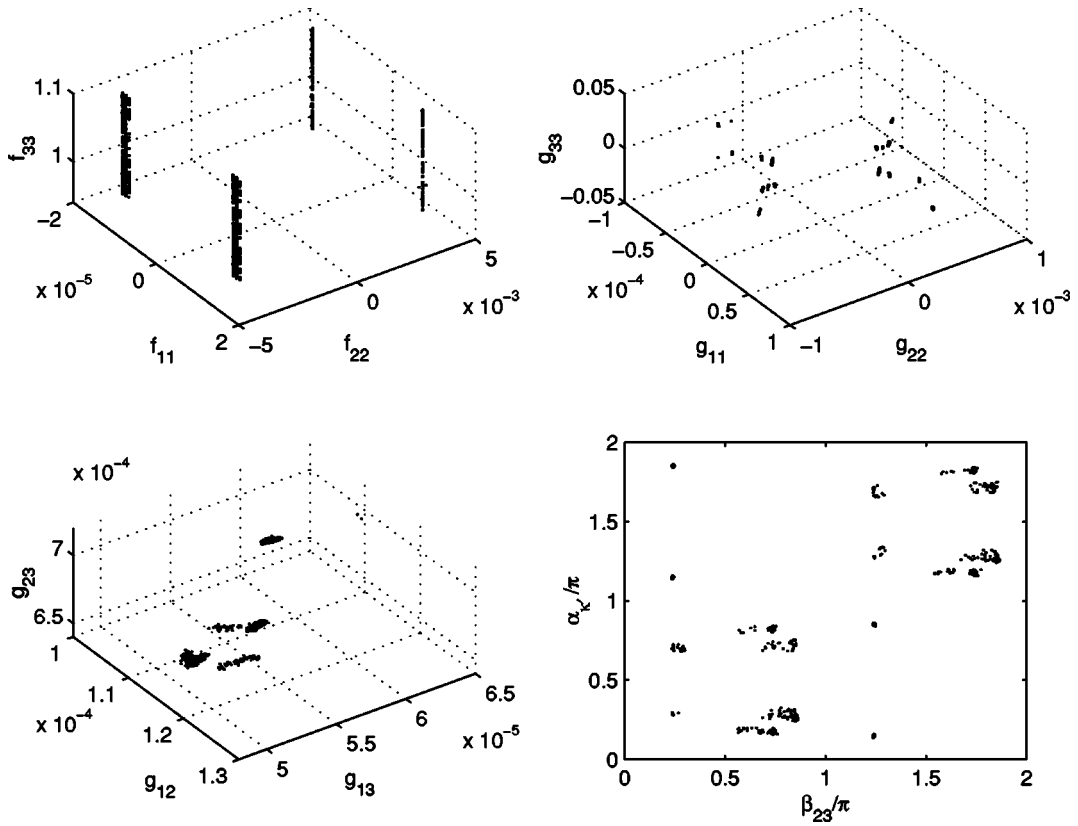

FIG. 7. Regions of the input parameter space that yield level II solutions when $M_2 = 5$ TeV and $M_H = 10$ TeV.

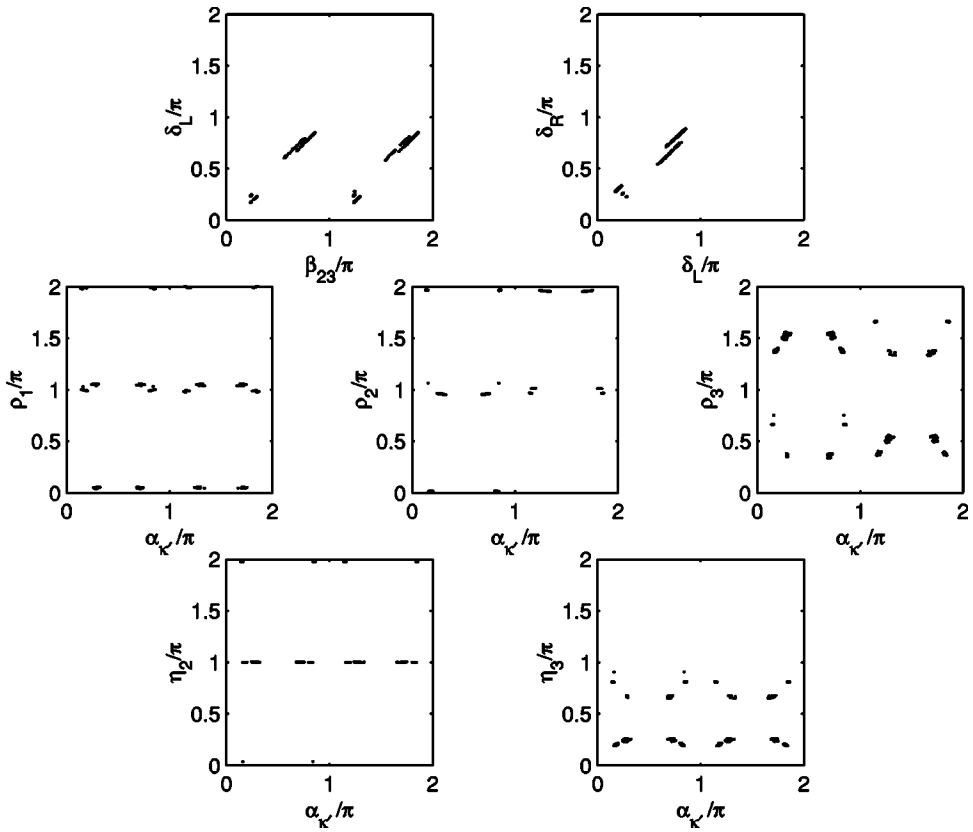

FIG. 8. Left- and right-handed CKM phases for the set of input parameters in Fig. 7. These are level II solutions with $M_2=5$ TeV and $M_H=10$ TeV.

remainder of our analysis. We have only discussed it in the present subsection in order to facilitate a comparison with the work in Ref. [20].[12]

B. A case study: $M_2=5$ TeV and $M_H=10$ TeV

We turn now to a case study for a particular pair of W_2 and Higgs boson masses, choosing $M_2=5$ TeV and $M_H=10$ TeV. Figures 7–10 show our numerical results for level II solutions in this case. Figure 7 contains a plot of the input parameter space showing points that satisfy the level II constraints when $M_2=5$ TeV and $M_H=10$ TeV. This figure may be compared with Fig. 1, which shows a set of points that pass only the level I constraints. Note that there are severe constraints on the possible values for $\alpha_{\kappa'}$ and β_{23}. In particular, both the quasimanifest ($\alpha_{\kappa'}=n\pi$) and pseudomanifest ($\beta_{23}=n\pi$) limits would appear to be ruled out for this particular pair of values for the masses M_2 and M_H. Figure 8 shows the left- and right-handed CKM phases for the set of input parameters in Fig. 7. This figure may similarly be compared with Fig. 3. The level II constraints rule out most of the possible values that the right-handed phases could in principle assume. Figure 9 shows frequency distributions for the five quantities yielding the level II constraints. The dashed vertical lines indicate experimental and/or theoretical bounds in each case. The histogram plot in Fig. 10 shows the frequency distributions for each of the five short-distance contributions to ϵ_K. The SM, FCNH and W_1-W_2 contributions can all be quite significant. Some further investigation has also shown a relatively strong anticorrelation between the FCNH and W_1-W_2 contributions that yield level II solutions: when the contributions are large they tend to be of opposite sign.

C. The generic case: variable masses

Figures 11–13 show the results obtained when M_2 and M_H are allowed to vary over prescribed ranges. Level II solutions were found for Higgs boson masses as low as about 7 TeV, despite the apparently dangerous tree-level FCNH

[12]We note here that the phenomenological estimates of ϵ'/ϵ have a very wide range within the context of the SM (see, e.g., Bertolini [37]). Not only does the calculation of the hadronic matrix elements of the relevant four-quark operators remain a formidable theoretical challenge, but this difficulty is considerably compounded by the fact that there are large cancellations between the contributions of the QCD penguin diagrams and the electroweak penguin diagrams. Recently, important advances have been made in the treatment of chiral symmetry on the lattice and this is facilitating several new efforts [38–40], but at present there are still significant sources of systematic errors that need to be brought under control. These advances do give one hope, however, that with another few years of effort one may be in a much better position to make use of the precise experimental results [41,42] to constrain theories of *CP* violation.

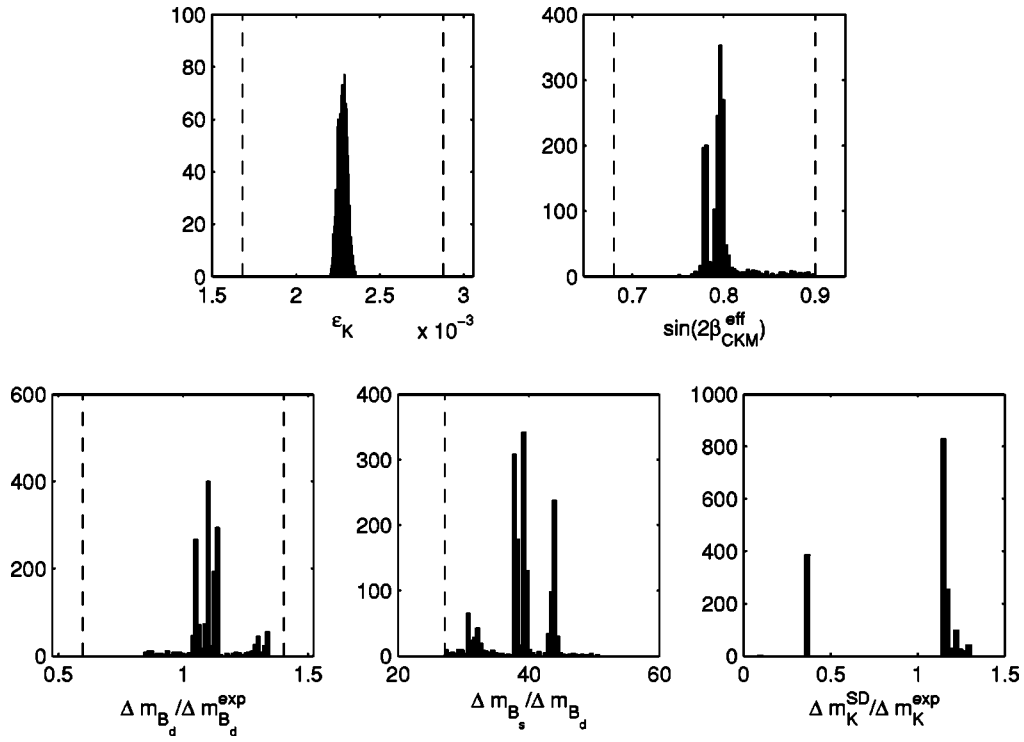

FIG. 9. Frequency plots of the five level II constraints for the data set in Fig. 7. The dashed vertical lines for ϵ_K, $\sin 2\beta^{\rm eff}_{CKM}$ and Δm_{B_d} indicate the theoretical and/or experimental uncertainties. The dashed line for Δm_{B_s} indicates the lower bound on $\Delta m_{B_s}/\Delta m_{B_d}$ [see Eq. (37)]. The data in the plot are level II solutions with $M_2=5$ TeV and $M_H=10$ TeV.

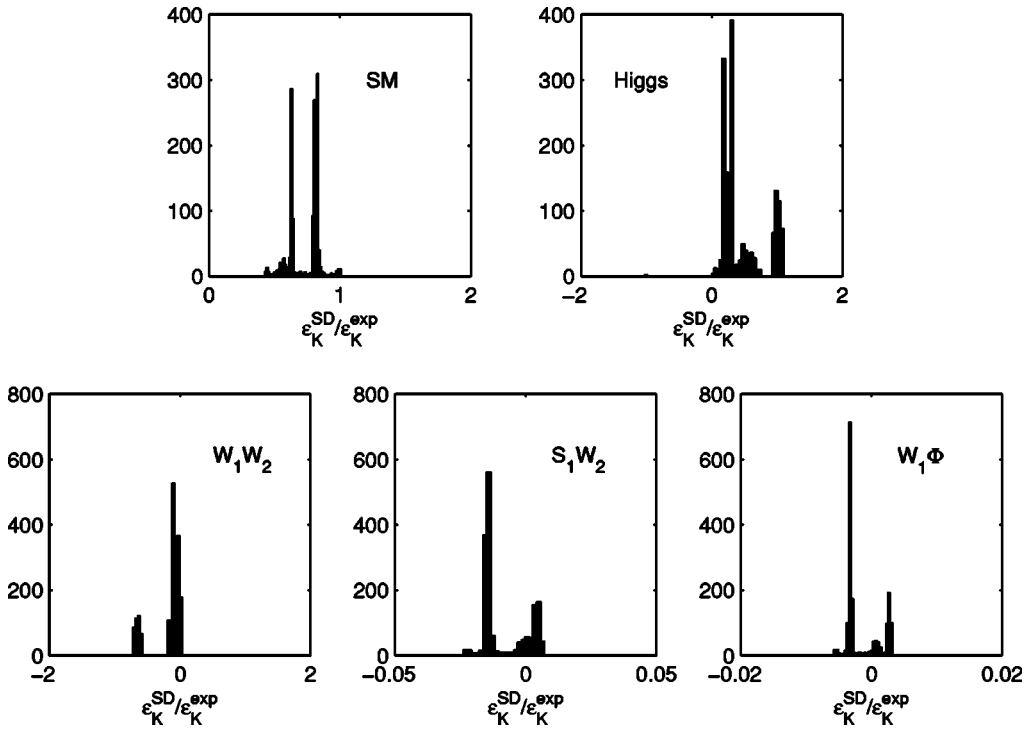

FIG. 10. Frequency plots of the five short-distance contributions to ϵ_K for the data set in Fig. 7. Note the different scales on the horizontal axes. The data in the plot are level II solutions with $M_2=5$ TeV and $M_H=10$ TeV.

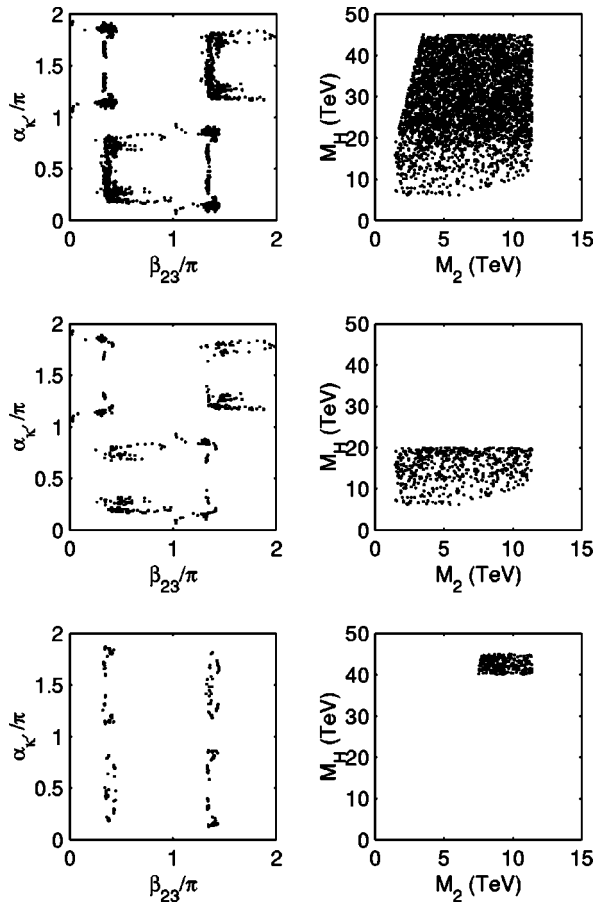

FIG. 11. Three pairs of plots showing level II solutions for the variable mass case. The plots on the right indicate the mass ranges under consideration and the plots on the left show the corresponding values of $\alpha_{\kappa'}$ and β_{23}. The middle and lower pairs of plots show subsets of the data contained in the upper pair of plots.

contribution in Eq. (41). Solutions were also found for W_2 masses as low as about 1.5 to 2 TeV. In choosing the masses we have employed the restrictions $M_H > M_2$, $M_2 > 1.4$ TeV and $M_H > 5$ TeV (otherwise, approximations in some of our theoretical expressions begin to lose some accuracy) and $M_2 < 13 M_H$ (perturbativity bound [43]). We have also placed (somewhat arbitrary) upper limits on the W_2 and Higgs boson masses, as is evident in Fig. 11.

There are three sets of plots in Fig. 11. The top pair shows the entire range of Higgs boson and W_2 masses considered (on the right) and the values of $\alpha_{\kappa'}$ and β_{23} for which solutions were found (on the left). It would appear from this plot that the quasimanifest limit (real Higgs VEVs; $\alpha_{\kappa'} = n\pi$) is disfavored, at least for the range of masses considered in the plot. (The quasimanifest case can actually yield solutions in the decoupling limit; as we shall discuss below.) The middle pair of plots shows the case in which $M_H < 20$ TeV and indicates that for these ''moderate'' Higgs boson masses the solutions in the $\beta_{23} - \alpha_{\kappa'}$ plane form roughly horizontal bands. The pseudomanifest case (real F and G; $\beta_{23} = n\pi$) does not appear to be ruled out, but does seem at least to be slightly disfavored. (Recall that we could in principle come to different conclusions than Ball *et al.*, since we do not use the ϵ' constraint in our analysis.) The bottom pair of plots in Fig. 11 shows the approach to the ''decoupling limit'' ($M_H, M_2 \to \infty$). In the decoupling limit the nonstandard contributions all tend to zero, leaving only the SM contribution. In contrast with the SB-LR, our model survives into this limit, since the usual left-handed phase δ_L can be made to take on any value in our model by choosing a suitable value for β_{23} [see Eq. (30) and Fig. 3], whereas δ_L is quite close to either 0 or π in the SB-LR.[13] Some additional investigation into the decoupling limit has shown that approximately vertical bands of solutions develop in the $\beta_{23} - \alpha_{\kappa'}$ plane in this limit. These bands are located near $\beta_{23}/\pi \simeq 0.4$ and $\beta_{23}/\pi \simeq 1.4$. (These values for β_{23} yield $\delta_L \simeq 1.2$ rad, which is just the usual result in the SM.) The beginnings of these vertical ''decoupling limit bands'' are evident in Fig. 11. Note that the decoupling limit version of Fig. 3 has very tightly constrained regions for δ_L and also for δ_R (the constraint on δ_R is due to the strong correlation between δ_R and δ_L).

Figure 12 shows the left-and right-handed phases in the variable mass case. Comparing with Fig. 3, we see that the level II constraints rule out many of the possible values that the phases could in principle assume. The restrictions are not as severe, however, as in the case considered in Fig. 8, where the W_2 and Higgs boson masses were fixed to be 5 and 10 TeV, respectively. Figure 13 displays the five short-distance contributions to ϵ_K (as fractions of $\epsilon_K^{\rm exp}$) in the variable mass case. Since many of the solutions actually correspond to quite large masses, the nonstandard distributions are all peaked around zero and the SM contribution is peaked around unity. Nevertheless, the data set includes cases in which the FCNH and $W_1 - W_2$ contributions are relatively large (and typically of opposite sign).

VII. DISCUSSION AND CONCLUSIONS

The left-right model provides a viable and aesthetically pleasing extension of the SM. We have presented a relatively exhaustive numerical investigation of a nonmanifest ''top-inspired'' version of the left-right model in which the Higgs VEVs are taken to be in the ratio $m_b : m_t$. This version of the model is very attractive in that it quite naturally reproduces the quark mass and rotation angle hierarchies. It has often been the case in the past that studies of the nonmanifest left-right model have relied on various *ansätze* regarding the form of the right-handed CKM matrix. In the present work we have solved for this matrix numerically. Our numerical work has yielded the intriguing result that the right-handed rotation angles and the phase δ_R are very similar in size to their left-handed counterparts. These relations have been corroborated analytically in Appendix B. One interesting feature

[13]Note that among the two fundamental *CP*-violating phases $\alpha_{\kappa'}$ and β_{23}, the contribution from $\alpha_{\kappa'}$ to the CKM phase δ_L is Cabibbo-suppressed by $\lambda = 0.22$ relative to that from the phase β_{23}. Thus models with vanishing β_{23} (such as the SB-LR) may not generate enough *CP* violation in general, and certainly not when the scale of new physics is very high (i.e., in the decoupling limit).

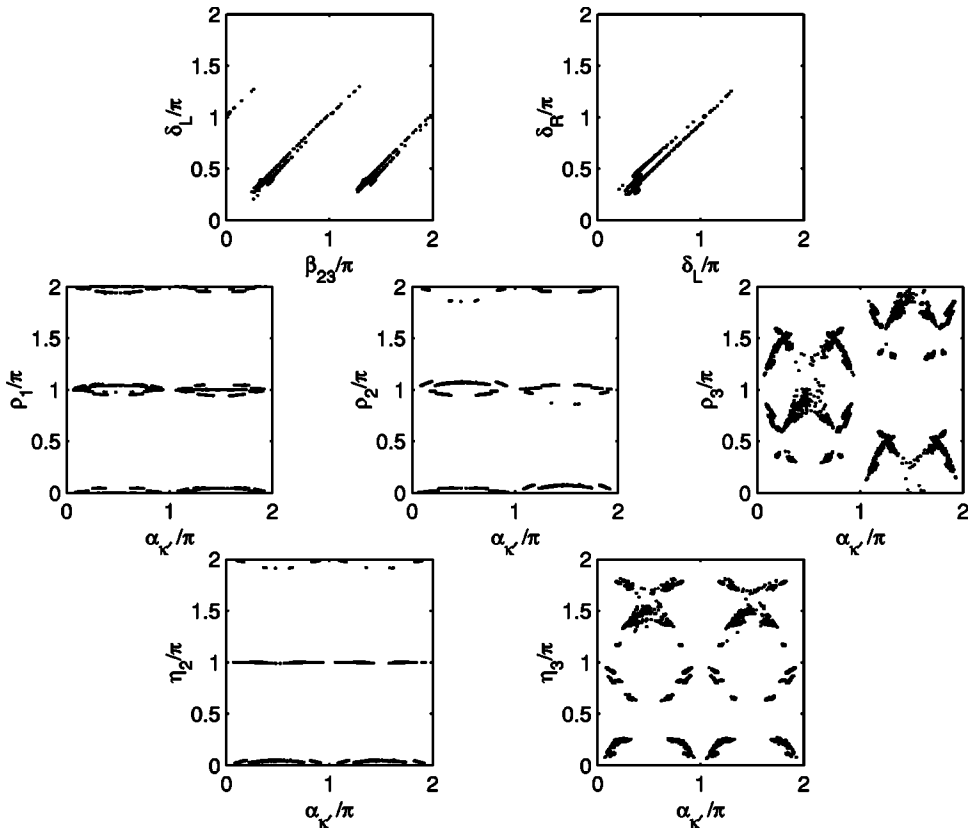

FIG. 12. Left-and right-handed CKM phases for level II solutions in the variable mass case. The data shown correspond to the mass range shown in the upper-right plot in Fig. 11.

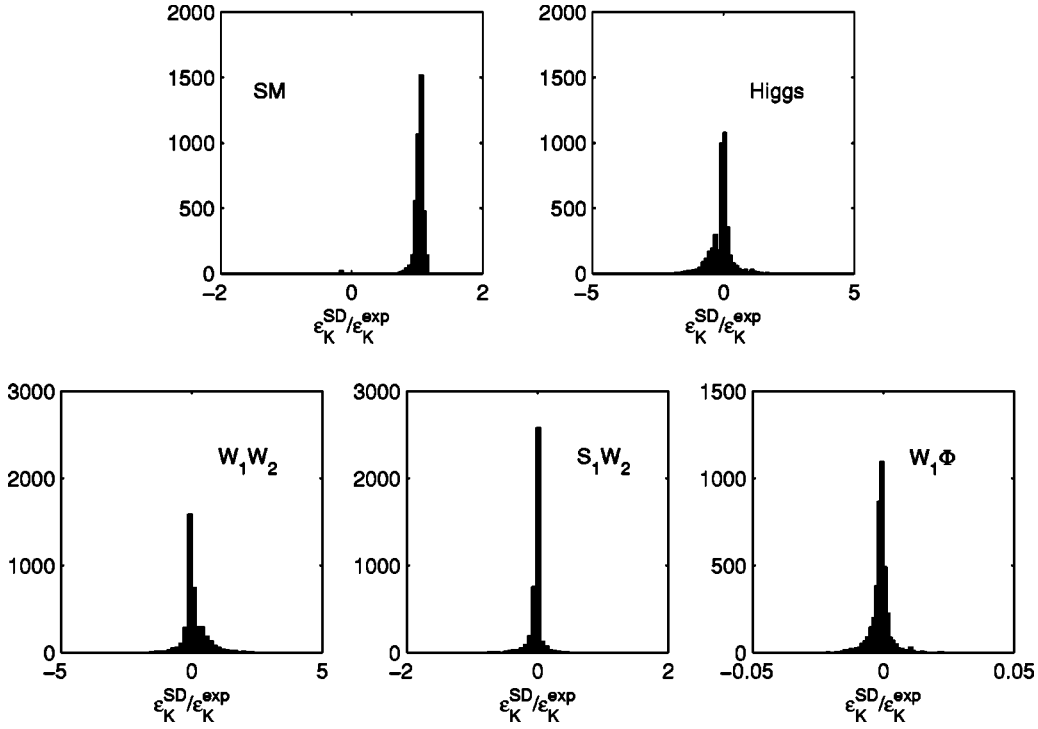

FIG. 13. Frequency plots of the five short-distance contributions to ϵ_K for the variable mass case.

of the model is that, unlike the SB-LR, it reduces to the SM in the decoupling limit.

One of the key insights in the present work is that unitary rotations may be used to rotate away many superfluous degrees of freedom in the quark Yukawa matrices F and G, yielding mass matrices that contain only two fundamental *CP*-odd phases. *CP*-violating quantities such as ϵ_K and $\sin 2\beta^{\rm eff}_{CKM}$ may then be used to place constraints on these two phases. Our numerical study indicates that the combined consideration of the neutral K and B systems leads to quite a strong reduction in the size of the available parameter space. In particular, the two *CP*-odd phases $\alpha_{\kappa'}$ and β_{23} are confined to rather small regions. From the vantage point of this numerical investigation, and with the range of masses considered here, it would appear that both the quasimanifest (real Higgs VEVs) and pseudomanifest (real Yukawa couplings) versions of the model are disfavored. The latter of these results is in agreement with recent work by Ball *et al.* [20], although some of our numerical results appear to be mildly different from theirs. One very intriguing result of the present work is that W_2 and Higgs boson masses as light as about 2 TeV and 7 TeV, respectively, are not inconsistent with current experimental constraints.

ACKNOWLEDGMENTS

We would like to thank Jeremy Case for helpful conversations and Jason O'Kane and Carl Daudt for technical assistance. This research was supported in part by the U.S. Department of Energy contract numbers DE-AC02-98CH10886 (BNL) and DE-FG03-96ER40969 (Oregon). K.K. and J.K. were supported by the Research Corporation and J.L. was supported by the SRTP at Taylor University. G.W. and K.K. would like to thank the BNL high energy theory group for its hospitality during the initial stages of this work.

APPENDIX A: ADAPTIVE MONTE CARLO ALGORITHM

The numerical solution of our model has been accomplished using an adaptive Monte Carlo algorithm. The goal of the algorithm is to find sets of input parameters $(f_{ii}, g_{ij}, \ldots)$ that satisfy the level I or level II constraints to within some required tolerance. Table I lists the various constraints employed and Eqs. (27) and (28) give the definitions of χ^2 for level I and II constraints, respectively. The basic procedure is to generate random values for the various input parameters (see Table II) and then to ''zoom in'' on a solution by searching for small values of χ^2. The procedure consists of $N_{\rm it}$ iterations (or ''zooms''), with each iteration consisting of the construction and diagonalization of $N_{\rm calc}$ separate sets of mass matrices. For each successive iteration, the sizes of the input parameter ranges are reduced and are centered on the ''best'' (as determined by χ^2) set of input parameters for the run so far. For a typical run, $N_{\rm calc}\sim 15$ and $N_{\rm it}\sim 5000$.

The specific procedures for generating level I and II solutions differ slightly; these differences are explained below after the description of the general algorithm. The general algorithm for finding a solution is as follows:

(1) For the nth iteration ($n=0,1,2,\ldots N_{\rm it}$), randomly generate a set of values for the relevant input parameters x_i (see Table II) within the ranges

$$x_{i,n}^{\rm cent} \pm \xi_n \Delta_i , \tag{A1}$$

where

$$\xi_n = \begin{cases} 1, & n=0, \\ (1.5n)^{-1}, & n>0. \end{cases} \tag{A2}$$

The above functional form for ξ_n was found to be convenient and relatively efficient. One could in principle choose a form for ξ_n that decreases more quickly (exponentially, say), but we were not successful in getting such forms to converge to solutions.[14]

(2) Numerically diagonalize the mass matrices (see Sec. II A) and determine the quark masses and the right- and left-handed CKM matrices.

(3) Evaluate the appropriate χ^2 (either $\chi^2_{(I)}$ or $\chi^2_{(II)}$) for the set of input parameters [see Eqs. (27) and (28)].

(4) Return to step (1) and repeat the process $N_{\rm calc}$ times. Keep track of the set of input parameters that has yielded the lowest value of χ^2 for the run so far, calling this set $\{x_i^{\rm best}\}$.

(5) After repeating the process $N_{\rm calc}$ times, set the ''central values'' of the various input parameters for the next iteration to the values that have yielded the best χ^2 so far for the run:

$$x_{i,n+1}^{\rm cent} = x_i^{\rm best} . \tag{A3}$$

Increment n by one and return to step (1). Repeat the entire process $N_{\rm it}$ times. Note that on returning to step (1), n has increased, so ξ_n has been reduced in size.

(6) Check the individual χ_i^2 once all $N_{\rm it}$ iterations are completed. If each of the $\chi_i^2 \leqslant 1$, the input parameter set is a solution.

A few modifications were made to the above procedure in order to increase its efficiency. For example, it was found empirically that χ^2 decreased rather quickly on runs that actually resulted in a solution. We thus modified the procedure so that runs were abandoned if χ^2 had not decreased below some threshold value after a specified number of iterations.

1. Level I solutions

As noted in Sec. IV, the six quark masses and three rotation angles provide nine essential constraints on the input parameter space. As a result, level I solutions may be found for any pair of phases $\alpha_{\kappa'}$ and β_{23} (the nine constraints simply act to constrain the nine input parameters f_{ii} and g_{ij}). In fact, in the limit that $\chi^2_{(I)} \to 0$, there appear to be 32 solutions for each pair of values of $\alpha_{\kappa'}$ and β_{23}. In searching for a level I solution, only the f_{ii} and g_{ij} are ''zoomed in upon;'' $\alpha_{\kappa'}$ and β_{23} are fixed at the beginning of a particular run and

[14]Since our routine allows the f_{ii} and g_{ij} to ''wander'' out of their original ranges, extra precautions were taken to ensure that f_{33}, g_{12}, g_{13} and g_{23} all remained positive.

are not altered throughout the course of the run. The level I solutions for Figs. 1–4 were generated by setting $N_{\rm calc}=15$ and $N_{\rm it}=1700$. Slightly modified procedures were used to generate the data for Figs. 5 and 6.

2. Level II solutions

In order to find a level II solution, one must specify values for M_2 and M_H (since ϵ_K, etc., depend on these). As level II solutions involve the addition of several new constraints compared to level I solutions, it is convenient to allow both $\alpha_{\kappa'}$ and β_{23} to be free parameters while zooming in on a solution. M_2 and M_H, however, may remain fixed for any particular run.

A few slight modifications must be made to the general algorithm when searching for a level II solution, since a straightforward application of the algorithm does not seem to lead to solutions. The reason for the problem appears to be the inclusion of ϵ_K in the evaluation of $\chi^2_{(II)}$. ϵ_K is strongly suppressed in the SM due in part to the presence of small CKM matrix elements [36]. At the beginning of a particular run, ϵ_K would typically be orders of magnitude too large because the elements in the CKM matrix would not initially have the correct hierarchy. A similar problem occurs for the right-handed contributions to ϵ_K. The massive deviation of ϵ_K from its experimental value at the beginning of a run leads to a very large contribution to χ^2 and upsets the zooming process. In order to get around the problem, we substitute approximate values (close to the known experimental values for the left-handed angles) for both the left- and right-handed rotation angles when determining the contribution of ϵ_K (and also of $\sin 2\beta^{\rm eff}_{CKM}$) to $\chi^2_{(II)}$ for the first several hundred iterations. At some point in each run a switch is made such that the true numerical versions of the left- and right-handed CKM matrices are used. (Note that part of the reason for the success of this trick is the relatively good agreement between the left- and right-handed rotation angles evident in Fig. 4.) The level II solutions for Figs. 7–13 were generated by setting $N_{\rm calc}=18$ and $N_{\rm it}=8000$.

APPENDIX B: ROTATION ANGLE AND PHASE RELATIONS IN THE MODEL

In this appendix, we derive analytical relations between the left- and right-handed rotation angles and the CKM phases δ_L and δ_R for the model considered in this paper. The analysis is greatly simplified by the smallness of the ratio of the VEVs: $|\kappa'/\kappa|=m_b/m_t$.

1. Angle relations

As discussed in Sec. II, the quark mass matrices in this model exhibit a surprising simplicity due to the hierarchy of the VEVs of the scalar bidoublet. In particular, $\mathcal{M}_u=\kappa F+\kappa'^* G$ is nearly diagonal in our choice of basis, and its small rotation angles can be safely neglected compared to the corresponding CKM rotations; i.e.,

$$|V_L^U|\simeq|V_R^U|\simeq \mathrm{diag}(1,1,1). \tag{B1}$$

Thus, both left-handed (LH) CKM rotations and right-handed (RH) rotations arise solely from $\mathcal{M}_d=\kappa' F+\kappa^* G$. Note that $\mathcal{M}_d$ is neither Hermitian (due to the phase $\alpha_{\kappa'}$) nor symmetric (due to the phase β_{23}), and we need two separate unitary rotation matrices V_L^D and V_R^D to diagonalize $\mathcal{M}_d$. We will show in this section that the LH and RH rotation angles are closely related in this model due to the hierarchical structure in the observed quark mass spectrum and in the CKM angles. This feature of the model is evident from the numerical results presented in the text.

We start by noting the approximate but useful hierarchies, $m_u:m_c:m_t\sim\lambda^8:\lambda^4:1$, $m_d:m_s:m_b\sim\lambda^4:\lambda^2:1$, and $V_{ub}\sim\lambda^4$, $V_{cb}\sim\lambda^2$, $V_{us}=\lambda=0.22$. $\mathcal{M}_d\mathcal{M}_d^\dagger$ is determined to a good approximation from the LH CKM matrix, with the order of magnitude of the different matrix elements given by

$$|\mathcal{M}_d\mathcal{M}_d^\dagger|\sim m_b^2\begin{pmatrix}\lambda^6&\lambda^5&\lambda^4\\ \lambda^5&\lambda^4&\lambda^2\\ \lambda^4&\lambda^2&1\end{pmatrix}. \tag{B2}$$

The hierarchical structure of this matrix will be useful as we examine the rotation angles.

The matrix $\mathcal{M}_d$ can be rewritten as

$$\mathcal{M}_d=H+P\simeq H+me^{i\alpha_{\kappa'}}\begin{pmatrix}0&0&0\\0&0&0\\0&0&1\end{pmatrix}, \tag{B3}$$

where $H=\kappa^* G$ is Hermitian, $m=|\kappa' f_{33}|\sim m_b$, and $P=\kappa' F$ and has been approximated by neglecting the small (1,1) and (2,2) elements for simplicity of analysis. The inclusion of all 3 diagonal elements of P is straightforward and does not affect our result. The LH and RH rotation matrices can be separately determined from $\mathcal{M}_d\mathcal{M}_d^\dagger$ and $\mathcal{M}_d^\dagger\mathcal{M}_d$, respectively:

$$\mathcal{M}_d\mathcal{M}_d^\dagger=(H+P)(H+P^*)\simeq\begin{pmatrix}H_{11}^2&H_{12}^2&H_{13}^2+e^{-i\alpha_{\kappa'}}H_{13}m\\ H_{21}^2&H_{22}^2&H_{23}^2+e^{-i\alpha_{\kappa'}}H_{23}m\\ H_{31}^2+e^{i\alpha_{\kappa'}}H_{31}m&H_{32}^2+e^{i\alpha_{\kappa'}}H_{32}m&H_{33}^2+m^2+2\cos\alpha_{\kappa'}H_{33}m\end{pmatrix}, \tag{B4}$$

$$\mathcal{M}_d^\dagger\mathcal{M}_d=(H+P^*)(H+P)=\mathcal{M}_d\mathcal{M}_d^\dagger(\alpha_{\kappa'}\to-\alpha_{\kappa'}) \tag{B5}$$

where H^2_{ij} denotes the (i,j) element of H^2. Therefore, the LH and RH rotation angles are also related by $\alpha_{\kappa'} \to -\alpha_{\kappa'}$, and for this reason, one would expect them to be of the same order of magnitude; i.e.,

$$\theta^L_{ij}/\theta^R_{ij} = \mathcal{O}(1). \tag{B6}$$

We thus arrive at the hierarchical structure of the $\mathcal{M}_d$ (thus H) matrix,

$$|\mathcal{M}_d| \sim m_b \begin{pmatrix} \lambda^4 & \lambda^3 & \lambda^4 \\ \lambda^3 & \lambda^2 & \lambda^2 \\ \lambda^4 & \lambda^2 & 1 \end{pmatrix} \sim |H|, \tag{B7}$$

where only the order of magnitude of each matrix element is given. To be more precise, $0 \leqslant |H_{33}|/m_b \leqslant \mathcal{O}(1)$, and this is because $|P_{33}| = |\kappa' f_{33}| \sim m_b$. We have checked that Eqs. (B9), (B12), and (B14) are valid even when $|H_{33}|/m_b \ll 1$.

Due to the hierarchical structure of $\mathcal{M}_d\mathcal{M}_d^\dagger$ [see Eq. (B2)], the LH angle θ^L_{23} (i.e., $|V_{cb}|$) is simply given by [44]

$$\theta^L_{23} \simeq \left| \frac{(\mathcal{M}_d\mathcal{M}_d^\dagger)_{23}}{(\mathcal{M}_d\mathcal{M}_d^\dagger)_{33}} \right| = \left| \frac{H_{23}H_{33} + H_{22}H_{23} + H_{21}H_{13} + e^{-i\alpha_{\kappa'}}H_{23}m}{(\mathcal{M}_d\mathcal{M}_d^\dagger)_{33}} \right|. \tag{B8}$$

It is easy to see that $(\mathcal{M}_d\mathcal{M}_d^\dagger)_{33}$ is even under $\alpha_{\kappa'} \to -\alpha_{\kappa'}$. In the numerator in Eq. (B8), only H_{23} and $e^{-i\alpha_{\kappa'}}$ are complex. If we ignore the small term of $H_{21}H_{13}$, we can then factor out H_{23} and observe that the numerator (thus θ^L_{23}) is invariant under $\alpha_{\kappa'} \to -\alpha_{\kappa'}$. Thus $\theta^R_{23} = \theta^L_{23}(\alpha_{\kappa'} \to -\alpha_{\kappa'}) \simeq \theta^L_{23}$. The inclusion of the small term $H_{21}H_{13}$ introduces a tiny correction to this equality relation,

$$\theta^R_{23} = \theta^L_{23} \times (1 + \mathcal{O}(\lambda^5)), \tag{B9}$$

where we have made use of Eq. (B7). This correction is of order 0.1% and is in good agreement with our numerical analysis (see the second plot in Fig. 4).

From Eq. (B2), one can reason that θ^L_{13} is given by

$$\theta^L_{13} \simeq \left| \frac{(\mathcal{M}_d\mathcal{M}_d^\dagger)_{13}}{(\mathcal{M}_d\mathcal{M}_d^\dagger)_{33}} \right| = \left| \frac{e^{-i\alpha_{\kappa'}}H_{13}m + H_{13}H_{33} + H_{12}H_{23} + H_{11}H_{13}}{(\mathcal{M}_d\mathcal{M}_d^\dagger)_{33}} \right|. \tag{B10}$$

Substituting the different terms with their orders-of-magnitude and phases, we have

$$\theta^L_{13} = |e^{-i\alpha_{\kappa'}} + \mathcal{O}(1) + e^{-i\beta_{23}}\mathcal{O}(\lambda)| \times \mathcal{O}(\lambda^4), \tag{B11}$$

which gives the right size for $|V_{ub}|$. The corresponding RH angle can then be deduced from θ^L_{13} with $\alpha_{\kappa'} \to -\alpha_{\kappa'}$, and we get

$$\theta^R_{13} = \theta^L_{13} \times (1 + \mathcal{O}(\lambda)). \tag{B12}$$

This $\mathcal{O}(\lambda)$ correction well explains the 20% fluctuation around unity in the third plot of Fig. 4.

The last step in the diagonalization of $\mathcal{M}_d\mathcal{M}_d^\dagger$ involves a (1,2) rotation. To first approximation, the matrix elements of the (1,2) submatrix are invariant under $\alpha_{\kappa'} \to -\alpha_{\kappa'}$, and we get

$$\theta^R_{12} \simeq \theta^L_{12}. \tag{B13}$$

To find out the correction to this relation, we need to include the "residual effect" on the (1,2) and (2,2) elements of $\mathcal{M}_d\mathcal{M}_d^\dagger$ from the (2,3) rotation. The (1,2) element is modified as

$$\begin{aligned} H^2_{12} &\to H^2_{12} + (H^2_{32} + e^{i\alpha_{\kappa'}}H_{32}m)(H^2_{13} + e^{-i\alpha_{\kappa'}}H_{13}m)/\mathcal{O}(m_b^2) \\ &= \{1 + \mathcal{O}(\lambda)e^{-i\beta_{23}}[e^{i\alpha_{\kappa'}} + e^{-i\alpha_{\kappa'}} + \mathcal{O}(1)] + \mathcal{O}(\lambda^2) \\ &\quad \times [e^{i\alpha_{\kappa'}} + \mathcal{O}(1)]\} \times \mathcal{O}(\lambda^5)m_b^2. \end{aligned}$$

Interestingly, the $\mathcal{O}(\lambda)$ term is invariant under $\alpha_{\kappa'} \to -\alpha_{\kappa'}$, and the leading noninvariant term appears at a higher order of λ^2.

One can similarly calculate the effect of the (2,3) rotation on the (2,2) element of $\mathcal{M}_d\mathcal{M}_d^\dagger$. We note that the noninvariant term under $\alpha_{\kappa'} \to -\alpha_{\kappa'}$ is of $\mathcal{O}(\lambda^5)$ relative to the invariant term. The LH rotation angle θ^L_{12} can now be calculated, and is given to first approximation by the ratio of the modified (1,2) and (2,2) elements. The RH angle θ^R_{12} can be obtained from θ^L_{12} with the substitution $\alpha_{\kappa'} \to -\alpha_{\kappa'}$. We thus get

$$\theta^R_{12} = \theta^L_{12} \times (1 + \mathcal{O}(\lambda^2)). \tag{B14}$$

The $\mathcal{O}(\lambda^2)$ correction nicely explains the $\sim$4% deviation from unity as presented in the first plot of Fig. 4.

Note that when either of the two phases vanishes, we have the exact relations $\theta^L_{ij} = \theta^R_{ij}$. In particular, when $\alpha_{\kappa'} = 0$ or π (quasimanifest case), $\mathcal{M}_d\mathcal{M}_d^\dagger = \mathcal{M}_d^\dagger\mathcal{M}_d$ because $P = P^*$. This yields identical LH and RH rotation angles. On the other hand, when $\beta_{23} = 0$ or π (pseudomanifest case), it is easily seen that the expressions for θ^L_{ij} are invariant under $\alpha_{\kappa'} \to -\alpha_{\kappa'}$, thus $\theta^L_{ij} = \theta^R_{ij}$.

2. Phase relations

Due to the hierarchical structure of the quark mass matrices in the model considered in this paper, we can use the triangular matrix technique developed in Ref. [44] to solve for the CKM phases δ_L and δ_R. In the triangular form, each mass matrix element has a simple correspondence with a quark mass or a rotation angle, and the CKM phases δ_L and δ_R are equal to linear combinations of the phases of certain elements of the up-and down-type quark mass matrices [44]. For practical purposes, $\mathcal{M}_u$ can be considered as diagonal in our model, and the CKM phase δ_L (δ_R) depends on the phases of four matrix elements of $\mathcal{M}_d$ rewritten in the upper (lower) triangular form [44].

For the purpose of comparing δ_L and δ_R later, Eq. (B7) can be rewritten with real and $\mathcal{O}(1)$ coefficients as follows:

$$\mathcal{M}_d \simeq m_b \begin{pmatrix} a_1\lambda^4 & a_2\lambda^3 & a_3\lambda^4 \\ a_2\lambda^3 & b_1\lambda^2 e^{id\lambda \sin\alpha_{\kappa'}} & b_2\lambda^2 e^{i\beta_{23}} \\ a_3\lambda^4 & b_2\lambda^2 e^{-i\beta_{23}} & e^{i\alpha'} \end{pmatrix}. \tag{B15}$$

Note that $m_b e^{i\alpha'} \equiv \kappa' f_{33} + \kappa^* g_{33}$, and that we have used α' to distinguish from $\alpha_{\kappa'} = \arg(\kappa')$. The $\mathcal{O}(\lambda)$ phase factor in $\mathcal{M}_d(2,2)$ comes from $\kappa' f_{22}$, and $d \simeq f_{22}|\kappa'|/(m_b\lambda^3 b_1)$ is an $\mathcal{O}(1)$ coefficient. On the other hand, $\kappa' f_{11}$ modifies $\mathcal{M}_d(1,1)$ by $1+\mathcal{O}(\lambda^4)$ and is thus neglected. For the phase relations, we will include corrections up to $\mathcal{O}(\lambda)$.

Consider first the phase δ_L in the LH CKM matrix. To this end, we apply RH rotations to Eq. (B15) to convert it to upper-triangular form,

$$\mathcal{M}_d \to \mathcal{M}_d^A \simeq m_b \begin{pmatrix} a_1'\lambda^4 & a_2\lambda^3 & a_3\lambda^4[1+c\lambda e^{i(\beta_{23}+\alpha')}] \\ 0 & b_1\lambda^2 e^{id\lambda \sin\alpha_{\kappa'}} & b_2\lambda^2 e^{i\beta_{23}} \\ 0 & 0 & e^{i\alpha'} \end{pmatrix}, \tag{B16}$$

where $c = a_2 b_2/a_3$, a_1 has changed to a_1' which itself carries an $\mathcal{O}(\lambda)$ phase, and higher-order corrections in λ are ignored.

The CKM phase δ_L can now be expressed in terms of four elements of $\mathcal{M}_d^A$ [44],

$$\delta_L \simeq \arg\left[\frac{\mathcal{M}_d^A(1,2)\mathcal{M}_d^A(2,3)}{\mathcal{M}_d^A(1,3)\mathcal{M}_d^A(2,2)}\right] \simeq \beta_{23} - c\lambda \sin(\beta_{23}+\alpha') - d\lambda \sin\alpha_{\kappa'} + n\pi, \tag{B17}$$

where $n\pi = \arg(a_2 b_2/a_3 b_1)$ and can be 0 or $\pm\pi$.

To obtain an expression for δ_R in the RH CKM matrix, we apply LH rotations to Eq. (B15) to convert it to lower-triangular form,

$$\mathcal{M}_d \to \mathcal{M}_d^B \simeq m_b \begin{pmatrix} a_1'\lambda^4 & 0 & 0 \\ a_2\lambda^3 & b_1\lambda^2 e^{id\lambda \sin\alpha_{\kappa'}} & 0 \\ a_3\lambda^4[1+c\lambda e^{-i(\beta_{23}-\alpha')}] & b_2\lambda^2 e^{-i\beta_{23}} & e^{i\alpha'} \end{pmatrix}. \tag{B18}$$

The phase δ_R can be similarly obtained,

$$\delta_R \simeq \arg\left[\frac{\mathcal{M}_d^B(2,2)\mathcal{M}_d^B(3,1)}{\mathcal{M}_d^B(2,1)\mathcal{M}_d^B(3,2)}\right] \simeq \beta_{23} - c\lambda \sin(\beta_{23}-\alpha') + d\lambda \sin\alpha_{\kappa'} + n\pi, \tag{B19}$$

where $n\pi = \arg(a_3 b_1/a_2 b_2) = \arg(a_2 b_2/a_3 b_1)$.

Some discussion is in order regarding several features and limits of the model.

(1) $\delta_R \approx \delta_L$. Comparing the expressions for δ_L and δ_R, we see that they differ only in the sign of $\alpha_{\kappa'}$ (thus α'), as noted when we examined the LH and RH angles. More specifically,

$$\delta_R = \delta_L + 2c\lambda \cos\beta_{23} \sin\alpha' + 2d\lambda \sin\alpha_{\kappa'} + \mathcal{O}(\lambda^2). \tag{B20}$$

Therefore, δ_R and δ_L become degenerate if $\alpha_{\kappa'} = 0$ or π. Noting that c, $d = \mathcal{O}(1)$ and $2\lambda = 0.44$, Eq. (B20) well explains our numerical relation of Eq. (31) and the second plot in Fig. 3,

$$\delta_R \approx \delta_L \pm 0.50 \text{ rad}.$$

In other words, δ_L and δ_R are equal up to $\mathcal{O}(\lambda)$ corrections from a nonzero $\alpha_{\kappa'}$.

(2) $\delta_L \approx \beta_{23} \approx \delta_R (mod\ \pi)$. As c, $d = \mathcal{O}(1)$ and $\lambda = 0.22$, we see that Eq. (B17) is in good agreement with our numerical relation of Eq. (30) and the first plot in Fig. 3:

$$\delta_L \approx \beta_{23} + n\pi \pm 0.25 \text{ rad}.$$

A similar expression is valid for δ_R. In both cases, the CKM phase is simply equal to β_{23} (mod π) up to $\mathcal{O}(\lambda)$ corrections. In particular, the contribution to $\delta_{L,R}$ from $\alpha_{\kappa'}$ is Cabibbo-suppressed by λ relative to that from β_{23}.

(3) *(Quasi)manifest limit.* $\delta_L = \delta_R$. In the limit $\alpha_{\kappa'} = 0$ or π (thus $\alpha' = 0$ or π), we recover the (quasi)manifest left-right symmetric model, and $\delta_L = \delta_R$ (exactly), as is well known for this scenario. For our model, we have

$$\delta_R = \delta_L \approx \begin{cases} \beta_{23} - c\lambda \sin\beta_{23} + n\pi & (\alpha' = 0), \\ \beta_{23} + c\lambda \sin\beta_{23} + n\pi & (\alpha' = \pi). \end{cases} \tag{B21}$$

(4) *Pseudomanifest limit (or SB-LR).* $\delta_R = -\delta_L$ *and* $|\delta_{L,R} - n\pi| \leqslant \mathcal{O}(\lambda)$. In the limit $\beta_{23} = 0$ or π, we have the pseudomanifest left-right symmetric model, or the SB-LR.

As is well known for this case, we have the exact relation $\delta_L = -\delta_R$. In our model, we get

$$\delta_R = -\delta_L \approx \begin{cases} c\lambda \sin\alpha' + d\lambda \sin\alpha_{\kappa'} + n\pi & (\beta_{23}=0), \\ -c\lambda \sin\alpha' + d\lambda \sin\alpha_{\kappa'} + (n+1)\pi & (\beta_{23}=\pi). \end{cases} \tag{B22}$$

Interestingly, the magnitudes of both phases are Cabibbo-suppressed, i.e.

$$|\delta_{L,R} - m\pi| \leqslant \mathcal{O}(\lambda) \quad (\beta_{23}=0 \text{ or } \pi), \tag{B23}$$

where $m=0$ or 1. Note that this suppression arises before we impose any *CP*-violating constraints on the model. Our analytical result is consistent with the numerical findings of Ball *et al.* [20],

$$|\delta_L - m\pi| \leqslant 0.25 \quad (m=0,1).$$

This Cabibbo-suppression of the CKM phases may help explain why the SB-LR is disfavored by the $\sin 2\beta^{\text{eff}}_{CKM}$ measurement.

[1] J. C. Pati and A. Salam, Phys. Rev. Lett. **31**, 661 (1973).
[2] R. N. Mohapatra and J. C. Pati, Phys. Rev. D **11**, 566 (1975).
[3] G. Senjanović and R. N. Mohapatra, Phys. Rev. D **12**, 1502 (1975).
[4] H. Fritzsch and P. Minkowski, Nucl. Phys. **B103**, 61 (1976).
[5] F. I. Olness and M. E. Ebel, Phys. Rev. D **30**, 1034 (1984).
[6] J. F. Gunion, J. Grifols, A. Mendez, B. Kayser, and F. Olness, Phys. Rev. D **40**, 1546 (1989).
[7] N. G. Deshpande, J. F. Gunion, B. Kayser, and F. Olness, Phys. Rev. D **44**, 837 (1991).
[8] P. L. Cho and M. Misiak, Phys. Rev. D **49**, 5894 (1994).
[9] L. Reina and M. Tytgat, Phys. Rev. D **50**, 751 (1994).
[10] G. Barenboim, M. Gorbain, U. Nierste, and M. Raidal, Phys. Rev. D **65**, 095003 (2002).
[11] Y. Rodriguez and C. Quimbay, Nucl. Phys. **B637**, 219 (2002).
[12] G. Beall, M. Bander, and A. Soni, Phys. Rev. Lett. **48**, 848 (1982).
[13] N. Cabibbo, Phys. Rev. Lett. **10**, 531 (1963).
[14] M. Kobayashi and T. Maskawa, Prog. Theor. Phys. **49**, 652 (1973).
[15] G. Ecker, W. Grimus, and W. Konetschny, Phys. Lett. **94B**, 381 (1980).
[16] G. Ecker, W. Grimus, and W. Konetschny, Nucl. Phys. **B177**, 489 (1981).
[17] G. Ecker and W. Grimus, Nucl. Phys. **B258**, 328 (1985).
[18] G. Ecker and W. Grimus, Z. Phys. C **30**, 293 (1986).
[19] J.-M. Frère *et al.*, Phys. Rev. D **46**, 337 (1992).
[20] P. Ball, J.-M. Frère, and J. Matias, Nucl. Phys. **B572**, 3 (2000).
[21] P. Ball and R. Fleischer, Phys. Lett. B **475**, 111 (2000).
[22] M. E. Pospelov, Phys. Rev. D **56**, 259 (1997).
[23] P. Langacker and S. U. Sankar, Phys. Rev. D **40**, 1569 (1989).
[24] Particle Data Group, D. E. Groom *et al.*, Eur. Phys. J. C **15**, 1 (2000).
[25] B. Aubert *et al.*, Phys. Rev. Lett. **87**, 091801 (2001).
[26] K. Abe *et al.*, Phys. Rev. Lett. **87**, 091802 (2001).
[27] T. Affolder *et al.*, Phys. Rev. D **61**, 072005 (2000).
[28] Y. Koide and H. Fusaoka, Phys. Rev. D **64**, 053014 (2001).
[29] G. Barenboim, J. Bernabéu, and M. Raidal, Nucl. Phys. **B511**, 577 (1998).
[30] M. Ciuchini *et al.*, J. High Energy Phys. **07**, 013 (2001).
[31] D. Atwood and A. Soni, Phys. Lett. B **508**, 17 (2001).
[32] A. Hocker *et al.*, Eur. Phys. J. C **21**, 225 (2001).
[33] The LEP B Oscillation Working Group, http://lepbosc.web.cern.ch/LEPBOSC/
[34] W.-S. Hou and A. Soni, Phys. Rev. D **32**, 163 (1985).
[35] D. Chang, J. Basecq, L.-F. Li, and P. B. Pal, Phys. Rev. D **30**, 1601 (1984).
[36] G. Buchalla, A. J. Buras, and M. E. Lautenbacher, Rev. Mod. Phys. **68**, 1125 (1996).
[37] S. Bertolini, hep-ph/0206095.
[38] CP-PACS Collaboration, J. I. Noaki *et al.*, hep-lat/0108013.
[39] RBC Collaboration, T. Blum *et al.*, hep-lat/0110075.
[40] See, e.g., the plenary talk given by L. Giusti at Lattice 2002, http://mitbates.mit.edu/lattice02/proceedings.html/
[41] V. Fanti *et al.*, Phys. Lett. B **465**, 335 (1999).
[42] A. Alavi-Harati *et al.*, Phys. Rev. Lett. **83**, 22 (1999).
[43] F. I. Olness and M. E. Ebel, Phys. Rev. D **32**, 1769 (1985).
[44] T. K. Kuo, S. W. Mansour, and G.-H. Wu, Phys. Lett. B **467**, 116 (1999).